IGF2BP1 restrains immunogenic endogenous dsRNA to suppress innate immune activation

Shaojun Zhang[1,‡], Wenze Huang[2,‡], Xiaoyu Meng[3,4,‡], Xu Yang[5], Pengfei Wang[2], Yifan Wei[2], Lei Tang[2], Yang An[3,4,§], Xiaoyu Hu[6,7,§], Qiangfeng Cliff Zhang[2,§]

[1] Ministry of Education Key Laboratory of Molecular and Cellular Biology; Hebei Research Center of the Basic Discipline of Cell Biology; Hebei Key Laboratory of Molecular and Cellular Biology; College of Life Sciences, Hebei Normal University, 050024 Shijiazhuang, China

[2] MOE Key Laboratory of Bioinformatics, Beijing Advanced Innovation Center for Structural Biology, Center for Synthetic and Systems Biology, Tsinghua-Peking Center for Life Sciences, School of Life Sciences, Tsinghua University, Beijing 100084, China

[3] Department of Biochemistry and Molecular Biology, College of Basic Medical Sciences; Shanxi Key Laboratory of Birth Defect and Cell Regeneration; MOE Key Laboratory of Coal Environmental Pathogenicity and Prevention, Shanxi Medical University, Taiyuan 030001, China

[4] Department of Plastic Surgery, Peking University Third Hospital, Beijing, 100191, China

[5] College of Life Sciences, Sichuan University, Chengdu 610065, China

[6] Institute for Immunology and School of Medicine, Tsinghua University, Beijing 100084, China

[7] Beijing Key Laboratory for Immunological Research on Chronic Diseases, Tsinghua University, Beijing 100084, China

[‡] These authors contributed equally to this work

[§] Correspondences: xiaoyuhu@tsinghua.edu.cn (X.H.), anyangdoctor@163.com (Y.A.), qczhang@tsinghua.edu.cn (Q.C.Z.)

Lead contact: qczhang@tsinghua.edu.cn (Q.C.Z.)

29 Running title: IGF2BP1 suppresses *Alu*-dsRNA immunogenicity

30 Keywords: IGF2BP1; RNA structure; Endogenous dsRNA; *Alu* elements; Self-RNA
31 tolerance; Innate immunity

32

Abstract

The accumulation of endogenous double-stranded RNA (dsRNA) triggers cytosolic innate immune response, yet how cells maintain tolerance to self-RNA remains incompletely understood. Here, we identify the oncofetal RNA-binding protein IGF2BP1 as a critical suppressor of endogenous dsRNA immunogenicity. Genetic ablation of IGF2BP1 in cancer cells and intestinal organoids caused the accumulation of immunogenic dsRNA, activated a viral-mimicry-like type I interferon response, and inhibited cell growth. Transcriptome-wide RNA-structure and protein–RNA interaction analyses showed that IGF2BP1 preferentially binds 3′-UTRs enriched in *Alu* elements and associates with the RNA helicase DHX9 and the adenosine deaminase ADAR1, two established regulators of endogenous dsRNA homeostasis. RNA isolated from IGF2BP1-deficient cells was sufficient to induce dsRNA-sensor expression in recipient cells, supporting the immunostimulatory potential of the accumulated RNA species. These findings establish IGF2BP1 as a regulator of self-RNA structural homeostasis and nominate its inhibition as a potential viral-mimicry-based strategy for cancer immunotherapy.

Introduction

The innate immune system serves as the first line of defense against pathogens and malignant transformation (Carpenter and O'Neill, 2024; Hu et al., 2024). A cornerstone of this defense is the type I interferon (IFN) response, triggered when pattern recognition receptors (PRRs) detect pathogen-associated or damage-associated molecular patterns. PRR activation drives the production of cytokines, such as IFN-β, followed by the subsequent expression of interferon-stimulated genes (ISGs), initiating antiviral and antitumor immune responses (Carpenter and O'Neill, 2024; Demaria et al., 2019; Hur, 2019). Double-stranded RNA (dsRNA) is a potent immunostimulatory signal recognized by cytosolic RIG-I-like receptors (RLRs). Although RLRs typically detect viral dsRNA, they can also be aberrantly activated by unresolved or exposed endogenous dsRNA. Failure to maintain tolerance to endogenous dsRNA can cause sterile inflammation and autoimmune disorders, including systemic lupus erythematosus and Aicardi-Goutières syndrome (Crow et al., 2019; Hofer et al., 2024). Conversely, cancer cells frequently co-opt RNA regulatory mechanisms to suppress endogenous dsRNA accumulation and evade innate immune surveillance (Tufail et al., 2025). Disrupting these protective pathways to reactivate IFN signaling has therefore emerged as a promising strategy to enhance antitumor immunity (Boukhaled et al., 2021; Liang et al., 2021; Sasaki et al., 2025).

RNA-binding proteins (RBPs) regulate nearly all aspects of RNA metabolism, including stability, translation, splicing, localization and structure of endogenous transcripts (He et al., 2023; Hentze et al., 2025). A growing number of RBPs, including DExD/H-box-containing RLRs, have been implicated in innate immune regulation and

disease progression (Panthi and Lynch, 2025; Turner and Petkau, 2026). However, how abundant RBPs regulate dsRNA homeostasis and innate immune activation remains poorly understood.

Insulin-like growth factor 2 mRNA-binding protein 1 (IGF2BP1) is a classic "oncofetal" RBP that is highly expressed in fetal tissues, nearly undetectable in most adult organs (Hammer et al., 2005), but frequently reactivated in diverse malignancies (Dhamdhere et al., 2023; Elcheva et al., 2020; Hagemann et al., 2023; Huang et al., 2018; Peng et al., 2025; Xiao et al., 2023). It contains two RNA-recognition motifs (RRMs) and four hnRNP-K homology (KH) domains, and promotes cell growth by controlling the stability, translation, and localization of target transcripts, including *MYC*, *ACTB*, *E2F1,* and *MAPK4* (Elcheva *et al.*, 2020; Hüttelmaier et al., 2005; Müller et al., 2020; Stöhr et al., 2012; Weidensdorfer et al., 2009), often acting as an N^6-methyladenosine (m^6A) reader (Müller et al., 2018; Xu et al., 2025).

Beyond these well-characterized post-transcriptional roles, emerging evidence points to an unexpected connection between IGF2BP1 and immune homeostasis. Systemic IGF2BP1 deficiency in mice causes perinatal lethality and abnormal intestinal morphogenesis (Hansen et al., 2004), conditional deletion in adult intestinal epithelial cells triggers acute colitis (Singh et al., 2020) and IGF2BP1 degradation in NSCLC cells elevates cellular innate immune responses (Li et al., 2021). Despite these provocative observations, the precise molecular mechanisms linking IGF2BP1 to innate immune regulation remain unknown, and whether this connection involves a direct role in dsRNA homeostasis has not been explored.

Here, we uncover a non-canonical function of IGF2BP1 as a critical regulator of endogenous dsRNA immunogenicity and innate immune evasion. We demonstrate that genetic depletion of IGF2BP1 in cancer cell lines and mouse intestinal organoids caused the accumulation of endogenous dsRNA, accompanied by activation of RIG-I, MDA5, IFN-β, and ISGs expression and marked inhibition of cancer cell proliferation. Mechanistically, we show that IGF2BP1 binds preferentially to *Alu* element-enriched 3′-UTRs and associates with the RNA helicase DHX9 and the A-to-I editing enzyme ADAR1 in the regulation of immunogenic dsRNA structures, thereby actively modulating the secondary structure of endogenous transcripts. These findings establish IGF2BP1 as a structural gatekeeper of self-RNA tolerance and innate immune evasion and nominate its inhibition as a potential therapeutic strategy for cancer immunotherapy.

Results

IGF2BP1 loss activates innate immune signaling and inhibits cell proliferation

To determine whether IGF2BP1 regulates innate immune homeostasis, we generated IGF2BP1-deficient Huh7 cells and characterized the resulting transcriptional response (Methods). Loss of IGF2BP1 strongly induced a type I interferon-associated program, including increased expression of RIG-I, MDA5 and numerous interferon-stimulated genes (ISGs, Fig. 1A-C; and Fig. S1A). This activation was not restricted to a single cell line: the protein level of RIG-I increased dramatically not only in Huh7 but also in HEK293 and HeLa IGF2BP1-knockout cells compared to wild-type cells (Fig. 1D). Importantly, re-expression of IGF2BP1 in knockout cells successfully rescued RIG-I levels (Fig. 1E), confirming that the immune activation is a direct consequence of

IGF2BP1 loss rather than a clonal artifact. Similarly, the mRNA level of MDA5 was upregulated more than 10-fold in IGF2BP1-knockout cells and this effect was completely reversed by IGF2BP1 re-expression (KO+IGF2BP1, Fig. 1F).

To investigate whether IGF2BP1 similarly restrains innate immune signaling in a more physiological context, we depleted IGF2BP1 in mouse intestinal organoids. This depletion robustly stimulated the expression of key innate immunity proteins, including RIG-I, MDA5, and PKR (Fig. 1G). In line with this activation, the production of cytokines, specifically IFNα and IFNβ, was significantly increased in IGF2BP1-KO cells (Fig. 1H). This immune activation was rescued by the re-expression of IGF2BP1 (KO+IGF2BP1), whereas knockdown of the control gene PPIA via short hairpin RNA failed to induce cytokine production (Fig. 1H), supporting a specific role for IGF2BP1 in restraining innate immune activation.

Having established that IGF2BP1 loss activates innate immune signaling across cell lines and organoids, we next assessed the functional consequences of this sustained immune activation. Depletion of IGF2BP1 in the liver cell line Huh7 via CRISPR/Cas9-mediated knockout (IGF2BP1-KO), or in the intestinal cell line Caco-2 via short hairpin RNA, severely repressed cell proliferation, whereas knockdown of PPIA had no significant effect on this phenotype (Fig. 2A-B). Direct treatment with recombinant IFN-β also inhibited the proliferation of both Huh7 and Caco-2 cells (Fig. 2A-B), recapitulating the phenotype of IGF2BP1 depletion and suggesting that interferon signaling may contribute to the growth defect.

The observation that IGF2BP1 loss induced an ISG program and interferon production, prompting us to compare this response with that elicited by a *bona fide* viral

challenge. To address this, we infected wild-type and IGF2BP1-knockout Huh7 cells with Zika virus (MR766). The ISG signature induced by IGF2BP1 deletion closely mirrored that of MR766 infection (Fig. 2C-E), with both conditions robustly stimulating *RIG-I* and *MDA5*. Strikingly, combining IGF2BP1 knockout with viral infection produced no additional increase in ISG expression in IGF2BP1-knockout cells (Fig. 2D), indicating that IGF2BP1 depletion had already strongly engaged the type I interferon pathway, largely recapitulating the transcriptomic state of viral infection. At the protein level, both IGF2BP1 knockout and MR766 infection increased innate immune proteins, whereas overexpression of IGF2BP1 suppressed these factors in infected cells (Fig. 1C, Fig. S1A). Collectively, these data identify IGF2BP1 as an endogenous suppressor of antiviral-like innate immune signaling and show that its loss induces a viral-mimicry-like cellular state.

IGF2BP1 loss causes the accumulation of immunogenic endogenous dsRNA

The induction of dsRNA sensors suggested that IGF2BP1 loss may lead to the accumulation of endogenous structured RNAs capable of stimulating innate immunity. To test this, we visualized dsRNA in IGF2BP1-KO cells using the dsRNA-specific antibody J2 (Schonborn et al., 1991). J2 immunofluorescence (IF) and dot-blot assays revealed significantly increased dsRNA in IGF2BP1-knockout Huh7 and HeLa cells relative to wild-type cells (Fig. 3A-B, Fig. S1A-B). Importantly, re-expressing IGF2BP1 in knockout Huh7 cells (KO+IGF2BP1) restored dsRNA levels (Fig. 3A-B), consistent with the reduction of RIG-I after IGF2BP1 re-expression (Fig. 1E).

To assess the effects of IGF2BP1 deletion on cellular RNA structures at a global scale, we performed RNA structure probing (icSHAPE) (Flynn et al., 2016) in wild-type and IGF2BP1-KO Huh7 cells. The resulting reactivity profiles showed high structural accuracy and reproducibility (Fig. S1C-E). Integrating these results with the IGF2BP1 binding sites identified by ultraviolet crosslinking and affinity purification (uvCLAP) (Maticzka et al., 2018) for IGF2BP1 in Huh7 cells (Fig. 4, Methods), we found that RNA regions directly targeted by IGF2BP1 exhibited significant structural alterations upon IGF2BP1 loss than non-target regions (Fig. 3C). Consistently, transcripts targeted by IGF2BP1 exhibited lower icSHAPE reactivity, consistent with increased base-pairing, in IGF2BP1-KO cells (Fig. 3D).

We asked whether RNA accumulated after IGF2BP1 loss was immunostimulatory. To test this, we enriched dsRNA from IGF2BP1-KO cells using the J2 antibody (J2-RNA) and transfected the recovered RNA into naïve HeLa cells. We found that J2-enriched RNA induced RIG-I expression in recipient cells (Fig. 3E). Similarly, transfection of total RNA from IGF2BP1-KO cells, but not from wild-type Huh7 cells, induced the expression of MDA5, RIG-I, and protein kinase R (PKR) (Fig. S1F). IGF2BP1 overexpression attenuated this response (Fig. S1F), further linking IGF2BP1 activity to protection against immunostimulatory RNAs.

To independently characterize the dsRNAs accumulating in IGF2BP1-deficient cells, we performed dsRNA immunoprecipitation and sequencing (dsRIP-Seq) (Gao et al., 2020). We found that more than 50% of the dsRNA pulled down by the J2 antibody were direct IGF2BP1 binding targets (Fig. 3F-G). Further, compared to IGF2BP1-WT cells, IGF2BP1-KO cells exhibited a global increase in complementary base-pairing within

these RNA regions (Fig. 3H-I). Taken together, these results show that IGF2BP1 loss increases endogenous dsRNA abundance and leads to the accumulation of RNA species capable of stimulating innate immune signaling. These accumulated dsRNAs represent candidate immunogenic ligands, although direct profiling of sensor-bound RNA will be required to establish their recognition by RIG-I or MDA5.

IGF2BP1 binds *Alu*-enriched 3'-UTRs and limits RNA duplex formation

To identify the RNA substrates through which IGF2BP1 regulates dsRNA homeostasis, we performed uvCLAP (Maticzka *et al.*, 2018) of IGF2BP1 in Huh7 cells (Methods). We found that IGF2BP1 predominantly binds to "CACA" motifs, with a strong preference for the 3'-UTR regions of target RNAs (Fig. 4A). The vast majority of IGF2BP1 targets (>96%) are mRNA (Fig. 4B), with associated genes enriched for pathways related to cell adhesion, viral infection, and translation (Fig. 4C). Compared to the binding profiles of PTBP1, another 3'-UTR binding protein, and TRA2A, an RRM-containing protein, a striking >44% of IGF2BP1-bound RNAs contain simple-repeats or *Alu* elements (Fig. 4D), two sequence classes with a strong propensity to influence RNA secondary structure (Masson et al., 2024; Setti et al., 2026; Smola et al., 2016; Yu et al., 2026).

Endogenous *Alu* elements can form double-stranded RNA (dsRNA) structures (Kim et al., 2016; Masson *et al.*, 2024). Under normal conditions, the cytosolic sensor like MDA5 do not recognize these cellular "self" dsRNAs (Ahmad et al., 2018; Hur, 2019; Sun et al., 2025). This natural tolerance is primarily due to post-transcriptional A-to-I editing by adenosine deaminases acting on RNA (ADARs), which disrupts the

perfect dsRNA duplex structure, making them unrecognizable to wild-type MDA5 (Ahmad *et al.*, 2018; Sun *et al.*, 2025). Typically, only mutated, hyperactive forms of MDA5 can overcome this tolerance to trigger an aberrant immune response against self-*Alu* RNAs. However, our data show that simply depleting IGF2BP1 is sufficient to robustly activate wild-type MDA5 and RIG-I (Fig. 1A-B, Fig. 2C-E). This raises a critical question: how does the loss of IGF2BP1 overcome this natural immune tolerance and activate the innate immune response against endogenous RNAs?

IGF2BP1 associates with DHX9 and ADAR1 to support endogenous dsRNA homeostasis

Our results indicate that IGF2BP1 contributes to endogenous RNA structural homeostasis, however, because IGF2BP1 lacks known helicase or enzymatic modification domains, we asked whether it associates with enzymes capable of remodeling structured RNA. By using affinity purification mass spectrometry (AP-MS) (Morris et al., 2014), we identified several DExD/H-box helicases interacting with IGF2BP1; in particular, DHX9 was highly enriched in the IGF2BP1 co-purification (Fig. 5A). We confirmed the interaction by co-immunoprecipitation (co-IP) (Fig. 5B, top). RNase A digestion markedly reduced the recovery of DHX9 co-immunoprecipitated with IGF2BP1, supporting that this interaction is RNA-dependent (Fig. 5B, top).

Interestingly, ADAR1 protein, which limits dsRNA immunogenicity through adenosine-to-inosine (A-to-I) editing, was also found to interact with IGF2BP1 (Fig. 5A). Loss-of-function mutations in ADAR1 cause spontaneous, pathogen-independent IFN production and Aicardi–Goutières syndrome through aberrant activation of MDA5 and

PKR (Rice et al., 2012) (Hu et al., 2023). We observed that, in contrast to DHX9, the interaction between IGF2BP1 and ADAR1 was enhanced by RNase treatment (Fig. 5B, second row), indicating that RNA modulates their interaction. Consistent with this model, intersection of the uvCLAP data of IGF2BP1 with known ADAR1 editing sites revealed that A-to-I editing sites within RNA frequently overlap with IGF2BP1 binding regions. Moreover, A-to-I editing increased after IGF2BP1 deletion (Fig. 5C). This increase may reflect greater availability or persistence of dsRNA substrates and a compensatory ADAR1 response, rather than impaired editing. Thus, these data associate IGF2BP1 with ADAR1 and edited RNA substrates but do not establish the direction or kinetics of ADAR1 recruitment.

Finally, we knocked down DHX9 or ADAR1 in Huh7 cells and measured cellular dsRNA by J2 immunofluorescence. Consistent with previous reports (Aktaş et al., 2017; Murayama et al., 2024), we observed a significant accumulation of dsRNA in DHX9-knockdown Huh7 cells (Fig. 5D). As expected, depletion of ADAR1 also led to the accumulation of dsRNA (Fig. 5D). In contrast, we observed no dsRNA accumulation in control PPIA-knockdown cells (Fig. 5D). Collectively, these results support a model in which IGF2BP1 functions within an RNA-remodeling network involving DHX9 and ADAR1. Whether these proteins form a coordinated complex or act on shared substrates through coordinated or parallel pathways remains to be established.

IGF2BP1 expression is associated with attenuated interferon signatures in human cancers

Having established experimentally that IGF2BP1 restrains endogenous dsRNA accumulation and interferon signaling, we asked whether this relationship was reflected in human tumors. We analyzed 16 TCGA cohorts containing at least ten matched tumor and adjacent non-tumor samples. IGF2BP1 mRNA were significantly elevated across multiple cancer types relative to matched non-tumor tissues (Fig. 6A; Fig. S2A-J). These included gastrointestinal, respiratory, reproductive and urinary malignancies. Across these cohorts, high IGF2BP1 expression (above the 75th percentile) was associated with poorer survival in COAD, STAD, LUAD, BRCA, and UCEC ($P < 0.05$) (Fig. 6B; Fig. S2K-N).

We next asked whether IGF2BP1 expression was associated with the innate immune landscape. In COAD, HCC, LUAD, and STAD patients, IGF2BP1-high tumors consistently showed lower expression of ISGs, including *IFIT5*, *IFIT2*, *OASL* and *GBP2* (Fig. S3A-D). This inverse relationship is not confined to individual tumor types: analysis of pan-cancer single-cell RNA-seq data (Kinker et al., 2020) and single cell RNA-seq data from TCGA revealed mutually exclusive expression patterns between ISGs and IGF2BP1 across multiple malignancies (Fig. 6C). These results suggest that IGF2BP1-mediated suppression of innate immune signaling is a general feature rather than a cancer-type-specific phenomenon.

We were particularly interested in genes encoding cytoplasmic dsRNA sensors, given their central role in initiating the type I interferon response that underpins anti-tumor immunity. Focusing on COAD, where we had the most comprehensive

transcriptomic data, we found that the expression levels of the dsRNA sensor-coding genes *RIG-I* (also known as *DDX58*) and *MDA5* (*IFIH1*) were upregulated in patients with low IGF2BP1 expression (Fig. 6D-E). A similar inverse correlation between IGF2BP1 and dsRNA sensor expression was observed in OV and HNSC patients (Fig. S4A-B), reinforcing the generality of this relationship.

Notably, this inverse relationship extends beyond cancer: *IGF2BP1* is significantly downregulated in patients with Crohn's disease (CD) and ulcerative colitis (Haberman et al., 2014), conditions in which the dsRNA sensor MDA5 was correspondingly upregulated (Fig. S4C-D), consistent with the observation that IGF2BP1 depletion in adult mouse intestines causes acute colitis (Singh *et al.*, 2020). Together, these analyses show that IGF2BP1-high tumors are associated with attenuated interferon-response signatures in several cancer cohorts. Because these relationships may be influenced by cancer type, purity, immune infiltration, proliferative state, and other clinical variables, they should be interpreted as clinical support for the experimentally defined mechanism rather than evidence that IGF2BP1 independently determines innate immune state or patient outcome.

Discussion

In this study, we identify a previously unrecognized function of IGF2BP1 in maintaining endogenous dsRNA homeostasis and suppressing aberrant innate immune activation. We show that IGF2BP1 binds preferentially to Alu-enriched 3′-UTRs, and its loss increases base pairing within target transcripts, promotes immunogenic dsRNA accumulation and induces a viral-mimicry-like interferon response in cancer cells and intestinal organoids.

These findings establish IGF2BP1 as a regulator of self-RNA structural homeostasis and expand its known functions beyond mRNA stability, localization and translation.

While IGF2BP1 is well-established as an "oncofetal" RNA-binding protein critical for fetal development and tumor progression, our analyses reveal a previously underappreciated dimension of its biology: an inverse association between IGF2BP1 expression and inflammatory gene signatures. This observation consistent with studies linking IGF2BP1 disruption to intestinal inflammation, including Crohn's disease and ulcerative colitis (Singh *et al.*, 2020) (Lim et al., 2015). Together, these observations support a broader role for IGF2BP1 in restraining innate immune activation, although they do not establish that IGF2BP1 independently determines inflammatory state or clinical outcome.

Integrated icSHAPE and uvCLAP analyses support a role for IGF2BP1 in RNA structural regulation. Over 40% of IGF2BP1 targets are enriched in *Alu* elements and simple repeats, sequences capable of forming base-paired secondary structures that resemble viral dsRNA (Athanasiadis et al., 2004). Under normal conditions, the A-to-I editing enzyme ADAR and RNA helicases like DHX9 resolve these structures to prevent autoinflammation (Aktaş *et al.*, 2017; Chung et al., 2018; Hu *et al.*, 2023; Sun *et al.*, 2025). The association of IGF2BP1 with both ADAR1 and DHX9 places it within a previously unrecognized RNA-remodeling network. We propose that IGF2BP1 binds specific 3′-UTR regions and supports DHX9- and ADAR1-associated regulation of adjacent Alu-dsRNA structures (Fig. 7).

By orchestrating this structural resolution, IGF2BP1 effectively acts as a gatekeeper of endogenous RNA immunogenicity. Rather than simply preventing the

initial folding of these RNAs, our data indicate that IGF2BP1 facilitates the active destabilization and editing of immunogenic dsRNA structures, thereby masking endogenous transcripts from detection by the cytosolic sensors RIG-I and MDA5. This mechanism operates in parallel with—and possibly upstream of—the established ADAR1-dependent self-tolerance pathway, suggesting that the dsRNA surveillance network is more layered than previously appreciated.

In the context of oncology, this function aligns with the emerging concept of "viral mimicry". Inducing the accumulation of endogenous dsRNA—often through epigenetic therapies like DNA methyltransferase (DNMT) inhibitors or RNA splicing modulators—triggers a robust interferon response that sensitizes tumors to immunotherapy (Bowling et al., 2021; Chiappinelli et al., 2015; Chomiak et al., 2024; Li et al., 2023; Stone et al., 2017). Our findings identify IGF2BP1 as a potential regulator of tumor-intrinsic viral mimicry. The frequent reactivation of IGF2BP1 in solid tumors may therefore serve as an adaptive mechanism to suppress endogenous dsRNA immunogenicity and evade innate immune surveillance, consistent with its strong association with poor clinical prognosis and therapy resistance.

Several important questions remain. First, while our *in vitro* and organoid models clearly demonstrate that IGF2BP1 loss activates dsRNA sensors and halts cancer cell proliferation, genetic perturbation of RIG-I, MDA5, MAVS and IFNAR signaling will be required to establish the pathways mediating these phenotypes. Second, investigating whether pharmacological inhibition of IGF2BP1 can synergize with immune checkpoint blockade (*e.g.*, anti-PD-1) by enhancing tumor intrinsic IFN production and infiltration of cytotoxic T-cells will be a vital next step. Third, exploring

the exact structural determinants that dictate IGF2BP1's affinity for specific *Alu*-containing transcripts may pave the way for targeted therapies aimed at selectively unmasking tumor-specific RNAs without triggering systemic autoimmunity. Finally, given that IGF2BP1 is largely absent from healthy adult tissues, its inhibition may offer a favorable therapeutic window, though potential effects on tissues with residual IGF2BP1 expression—such as the intestinal epithelium—will require careful assessment.

In summary, our study identifies IGF2BP1 as a regulator linking endogenous RNA structural homeostasis to innate immune quiescence. This non-canonical function expands the biological repertoire of IGF2BP1 beyond mRNA stabilization and translation. Its loss promotes the accumulation of immunostimulatory RNA structures and induces a viral-mimicry-like state. Future studies should determine whether this mechanism can be exploited therapeutically while preserving self-RNA tolerance in normal tissues.

Materials and Methods

Cell line and antibodies

Cell lines and antibodies used in this study are listed in Supplementary Table S1. All cell lines were determined to be free of mycoplasma based on PCR and nuclear staining. All cell lines mentioned in this study were cultured in DMEM (10% FBS, 1×Antibiotic-Antimycotic) under 37 ºC, 5% CO_2, except that C6/36 was cultured under 28ºC.

CRISPR knock out and short-hairpin RNA knock down

Guide RNAs were designed by using the CRISPOR (http://crispr.mit.edu). To generate IGF2BP1 knock out cell lines, two gRNA sequences were designed and cloned into the pX459 vector (Supplementary Table S1).

The gRNA-containing pX459 vectors were transfected into Huh7 cells using Lipofectamine 2000 (Invitrogen, 11668027) according to the manufacturer's instructions. The transfected cells were selected with puromycin for 3 days, surviving cells were digested with trypsin and diluted to 0.5 cells per 100 uL DMEM medium (10% FBS). The diluted cells were plated into 96 well plates for clonal selection. Mutations were identified by PCR sanger sequencing using the primers flanking the sites of gRNA targeting (Supplementary Table S1), and cells containing nonsense mutation were used for this study.

All short hairpin RNA (shRNA) plasmids were purchased from the MISSION shRNA Library (Sigma-Aldrich); full sequence identities of individual shRNA constructs were verified via Sanger sequencing using a U6 promoter sequencing primer. Lentiviral transduction was performed to establish stable cell lines harboring the aforementioned

shRNA clones. Following puromycin-based antibiotic selection (1 μg/ml), Huh7 and Caco-2 stable shRNA-expressing cells were seeded into 24-well and 96-well plates for cell proliferation assays and interferon ELISA measurements, respectively. Cell proliferation was quantified using a CCK-8 kit (YEASEN, 40203ES76), while interferon levels were determined with ELISA kits (Abcam, ab278127 and ab213479).

For genetic knockdown experiments in mouse intestinal organoids, organoid culture was performed following previously established protocols (Sato et al., 2009; Wang et al., 2025). Briefly, intestinal crypts were dissociated from fresh mouse small intestinal tissues via 30 min incubation at 4 °C in ice-cold PBS supplemented with 0.5 M EDTA. Isolated crypts were counted manually and centrifuged to obtain cell pellets. Approximately 500 crypts were resuspended in 30 μL of Matrigel (MedChemExpress, HY-K6007) and seeded into 24-well plates for culture. Intestinal organoids were maintained for 7 days in standard ENR culture medium containing recombinant growth factors, including 10–50 ng/mL EGF, 500 ng/mL R-spondin 1, and 100 ng/mL Noggin, as previously described (Sato *et al.*, 2009). For lentiviral shRNA transduction, organoids were mechanically dissociated into single cells and small cell clusters using the same procedure applied for routine organoid passaging. Dissociated organoid cells were resuspended in 10 mL of fresh ENR medium, mixed with lentiviral shRNA particles and 8 μg/mL polybrene (Sigma-Aldrich, TR1003), and incubated in 24-well plates at 37 °C for 16 h to facilitate viral transduction. Following transduction, cells were re-embedded in Matrigel and cultured under standard organoid growth conditions. Three days post-transduction, 2 μg/mL puromycin was added to the culture medium for continuous positive selection of stably transduced organoids. The survived organoids were routinely

401 passaged and expanded for subsequent experiments. The gene knockdown efficiency was
402 ultimately validated by western blotting analysis of the target protein.

403 **Immunofluorescence assay**

404 Huh7 cells were plated onto 12-well plate at 70% confluence and cultured for 12 hours
405 on microslides. Cells were washed 2 times with cold PBS, and fixed with cold absolute
406 methanol at -20°C. After washed with PBS, slides were blocked with 1% FBS
407 supplemented with 0.05% Tween-20. Antibodies used for detecting virial or host targets
408 are listed in Method. The nucleus was stained using DAPI. Fluorescence was monitored
409 by confocal microscopy (Nikon Ti-E) using the uniform parameter settings. The figures
410 were then analyzed and exported using NIS-Elements software (v4.30).

411 **RNA-seq**

412 Huh7 wild type and IGF2BP1 knocked out cells were plated onto a 15 cm dish at 50%
413 confluence before 12-hours that infection with ZIKV. 72-hours after infection (~70%-
414 80% cell confluence), medium was removed and cells were washed 2 times with ice-cold
415 PBS. A portion of cells were scraped, and RNA was extracted using RNAiso Plus
416 (TAKARA, 9109). Total RNA was subjected to RNA-seq library construction using
417 NEBNext Ultra RNA Library Prep Kit for Illumina (NEB, E7530S).

418 **RNA-seq data analysis**

419 RNA-seq data was de-duplicated with fastx-tool-kit firstly. Then the 5'/3'-adapter was
420 removed by Trimmomatic (v0.30). The cleaned reads were then mapped to rRNA index
421 with bowtie2 (v2.2.5). The unmapped reads were then mapped to human genome
422 (GRCh38.p10.genome.fa) and ZIKV genome with STAR (v2.7.0d). The number of

mapping reads of each gene was counted by featureCounts of the Subread package (v1.6.4). Gene annotations were extracted from GENCODE human GTF annotation file (GRCh38.gtf). The correlation of gene expression between different samples were calculated by using log10(reads counts + 1) of genes. edgeR was used for gene differential expression analysis. The following cut-offs were set for differentially expressed genes: FDR ≤ 0.05 and |fold change| ≥ 2. ggplot2 were used for volcano plots.

Identification IGF2BP1 binding targets using uvCLAP

PiggyBac transposon vectors expressing biotin ligase gene *BirA* and transposase (a kind gift from Xiaohua Shen Lab, Tsinghua University) were transfected into Huh7 cells and selected with hygromycin B to generate a cell line stably expressing *BirA*. The *Igf2bp1* open reading frame (ORF) was cloned from the cDNA of HEK293T cells, and fused with a 3*FLAG-biotinylation sequence (3fb) tag to the N-terminal of IGF2BP1 using overlap PCR. The 3fb-*Igf2bp1* ORF was then cloned into a pLVX-Puro vector with a CMV promotor and then transfected into the *BirA*-expressing Huh7 cell line using lentivirus, selected with hygromycin B (150 μg/ml) and puromycin (1 μg/ml). The 3fb-GFP expressing vector was also transfected into Huh7 cells as a control sample of uvCLAP.

uvCLAP of 3fb-IGF2BP1 was performed according to a previous report (Maticzka *et al.*, 2018). Briefly, cells were crosslinked by UV irradiation (150mJ/cm^2 at UV250). The crosslinked cells were lysed with 2 volumes (v/v) of lysis buffer (50mM Tris-HCl, pH 7.4; 300mM NaCl; 0.5% NP-40; 1% Triton X-100; 0.1% SDS). Total proteins were determined by the BCA method and 2 mg total proteins were used for each uvCLAP experiment. Cell lysate was firstly incubated with FLAG M2 Magnetic Beads (Sigma-Aldrich, M8823) for about 2h, then washed twice with lysis buffer and twice with

high salt wash buffer I (50mM Tris-HCl, pH 7.4; 1M NaCl; 0.5% NP-40). Then the protein-RNA complexes were eluted with 250 ug/mL 3*FLAG peptides (MACKLIN, X860819) in lysis buffer. The eluate was then incubated with MyOne C1 beads (Invitrogen,65001) to collect biotinylated IGF2BP1. After 3 hours' incubation, C1 beads were washed twice with SDS-Urea buffer (50mM Tris-HCl, pH7.4; 2% SDS; 4M Urea), twice high salt wash buffer II (5×PBS; 0.5% NP-40; 0.5% sodium deoxycholate; 0.1% SDS), following the twice wash with PNK buffer (50mM Tris-HCl, pH 7.4; 10mM $MgCl_2$; 0.5% NP-40). The pull-downed RNA was trimmed by MNase (NEB, M0247S) using a dilution ratio ranging from $1:10^4$ to $1:10^7$. Then, the trimmed RNA was dephosphorylated using CIP (NEB, M0290S) and the 3'-linkers were ligated to the RNA using T4 RNA Ligase 2, truncated KQ (NEB, M0373S). Excess free 3'-linkers were washed away with PNK buffer. Then the 3'-tagged RNA was released from beads by proteinase K digestion. 5'-linkers were ligated to the RNA using T4 RNA Ligase 1 (NEB, M0437M), and reversed transcribed using Superscript III (Invitrogen, 18080085). Linkers/adaptors and primers used for uvCLAP library construction are listed in Supplementary Table S1.

uvCLAP data analysis

For the uvCLAP-seq data, the 1st reads were used for further analysis. The 5'/3'-adapter of uvCLAP-seq data were removed by Trimmomaitc (v0.30). Sequencing data then was de-duplicated by using 6-bp unique molecular identifier in 5'-end. The cleaned reads were then mapped to rRNA index with bowtie2 (v2.2.5). The unmapped reads were then mapped to human and ZIKV genome with STAR (v2.7.0d). Peaks calling was produced

by Piranha (v1.2.1). uvCLAP-seq data tracks was produced by IGV (Integrative Genomics Viewer, v2.4.14).

IGF2BP1 eCLIP data from HepG2 and K562 cell lines (Van Nostrand et al., 2016) were used to compare with our uvCLAP data. For each transcript with IGF2BP1 binding peaks, we divided it into sliding windows (window size: 50nt, window step: 25nt) and calculated the mean reads depth of sliding windows. Then we calculated correlation of the mean reads depth of sliding windows between our data and previous eCLIP data. To search for the IGF2BP1 motifs, we selected the sequence of most significant 1000 IFG2BP1 binding peaks and call the motifs by using HOMER (v4.10) . For the metaplot, we divided each transcript 5'UTR, CDS and 3'UTR into 50 regions and calculated the mean peak sites of these regions. ggplot2 were used for making metaplot plots.

Double-stranded RNA detection, purification and transfection

For dsRNA immunofluorescence assay (IFA), mammalian cells were seeded on 12 well plate tilling glass slides with about 80% confluence. Cells were washed twice with PBS, fixed and permeabilized using 4% PFA in PBS containing 0.3% Triton-X100. Fixed cells were blocked using blocking buffer (5% FBS in PBS containing 0.3% Triton-X100) for about 2 hours at room temperature. J2 antibody (Scicons) was diluted as 1:2000 in blocking buffer and incubated with the fixed cells at 4 ºC for over-night. After PBS washes, cells were incubated with secondary antibody (Anti-Mouse IgG H&L Alexa Fluor 488, 1:2000 in blocking buffer containing 8ug/ml DAPI) at room temperature for 4 hours in dark. After PBS wash, the slides were mounted and observed under inverted microscope (Nikon, TS100) with UV405 and FITC models.

For dsRNA dot-blot, total RNA from Huh7 wild-type and IGF2BP1-KO cells were extracted using TRIzol reagent. Total RNA was diluted and 0.1, 0.5 and 1 μg RNA were blotted on nitrocellulose membrane. Then the membrane was blocked using blocking buffer (5% skim milk in TBST buffer) for over-night at 4 ºC. J2 antibody was diluted in blocking buffer (1:2000), and incubated with membrane at room for at least 4 hours. After washed with TBST buffer, secondary antibody (Goat Anti-Mouse IgG-HRP Conjugated) was incubated with membrane for 1 hour at room temperature. Finally, the membrane was developed using ECL reagent (Immobilon, WBKLS0500).

For cellular dsRNA purification, total RNA was extracted from Huh7 IGF2BP1-KO cells. 40 μg of total RNA was incubated in binding buffer (150 mM NaCl, 50 mM Tris-HCl pH 7.0, 1 mM EDTA, 0.5% NP-40) with 10 μg of J2 antibody and 10U SuperaseIn (Ambion, AM2696) overnight at 4 ºC. Then 50 μL of protein-A/G magnetic beads (Pierce, 88802) was added and incubated for 4 h at 4 ºC, followed by 5×washes in cold binding buffer. After last wash, beads were resuspended using 1 mL of TRIzol and the dsRNA was extracted as manufacturer's instructions. 350 μL supernatant was transferred for dsRNA precipitation using isopropanol. And the purified dsRNA was dissolved in 20 μL water.

Hela cells were seeded on 12 well plate with the confluence about 80%. J2-purified RNA or total RNA purified from cells was transfected into Hela cells using 2 μL Lipofectamine 2000 reagent (Thermo) as the manufacturer's instructions. Post 12 h of transfection, cells were collected for western-blot assay.

RNA structure probing experiments

Huh7 wild type and IGF2BP1 knocked out cell (4 plates for each cell line) were seed at ~80% confluence. Post 24 hours' seeding, 100mM NAI-N_3 were added to 2 plates for each cell line and incubated at 37 °C for 5 min with gentle mixing. Equal amounts of DMSO were added to another 2 plates for each cell line and used for control of NAI-N_3 modification. Then, cells were transferred immediately on ice for stopping modification. RNA was extracted using TRIzol reagent and purified with the Hipure RNA pure Micro Kit according to the manufacturer's instructions. icSHAPE sequencing library construction and sequencing data analyzing were performed according previous report (Flynn *et al.*, 2016).

Affinity purification mass spectrometry and co-immunoprecipitation

ORF of *Igf2bp1* fused with 3*FLAG tag was cloned into pLVX-Puro vector and co-transfected with packaging plasmids into HEK293T cells for lentivirus packaging. IGF2BP1 overexpressing Huh7 cells were generated by lentivirus transfection following puromycin selection. About 1×10^8 cells expressing 3*FLAG-IGF2BP1 were resuspended with lysis buffer (50 mM HEPES, pH 8.0, 100 mM KCl, 2 mM EDTA, 0.1% NP40, 5% glycerol, supplemented with protease inhibitor). The clarified lysates were incubated on ice or treated with RNase A (100μg/mL) at 25°C for 30min with shaking. Cell lysates of 3*FLAG-GFP were used for negative control. FLAG M2 beads (30μL) were added into the cell lysates and rotated at 4°C for 2h. Beads were washed twice using lysis buffer, followed two washes with high salt wash buffer (50 mM HEPES, pH 8.0, 0.5M KCl, 2 mM EDTA, 0.1% NP40, 5% glycerol). Proteins were eluted using FLAG peptides (200μg/mL) in lysis buffer. The eluted proteins were separated on SDS-PAGE gels and

534 visualized using silver staining. Protein bands on the gels were excised for mass
535 spectrometry assay (Thermo, Orbitrap Fusion).

536 Huh7 (1×10^8) cells were collected and resuspended using lysis buffer (25 mM
537 Tris-HCl, pH 7.5, 100mM NaCl, 1% NP40, and 0.5% sodium deoxycholate
538 supplemented with protease inhibitor). The clarified lysates were aliquot into two parts,
539 incubated on ice or treated with RNase A (100μg/mL) at 25°C for 30min respectively.
540 IGF2PB1 antibody (10 μg, MBL, RN007P) or rabbit IgG (10 μg) was conjugated to
541 100 μL protein A/G beads (Pierce, 88802). The conjugated beads were added to lysates
542 and rotated for 1h at 4 °C. Washed beads twice with lysis buffer and followed two washes
543 with high salt wash buffer (20 mM Tris-HCl, pH 7.4, 1M NaCl, 0.2% NP40
544 supplemented with protease inhibitor). The proteins were eluted using RIPA buffer
545 (20 mM Tris-HCl, pH 7.4, 100mM NaCl, 1% SDS and 50mM DTT). The eluted proteins
546 were separated on SDS-PAGE gels for western-blot analysis.

547

548 **Statistical analysis**

549 Data were analyzed using GraphPad Prism 6.01 (GraphPad Software, San Diego, CA,
550 USA) and R software. The values shown in the graphs are presented as means ± SD of at
551 least three independent experiments. Significance was determined by unpaired two-tailed
552 *t* test; $P < 0.05$ was considered statistically significant.

553

References

1. Ahmad, S., Mu, X., Yang, F., Greenwald, E., Park, J.W., Jacob, E., Zhang, C., and Hur, S. (2018). Breaching self-tolerance to Alu duplex RNA underlies MDA5-mediated inflammation. Cell *172*, 797-810.e713.
2. Aktaş, T., Avşar Ilık, İ., Maticzka, D., Bhardwaj, V., Pessoa Rodrigues, C., Mittler, G., Manke, T., Backofen, R., and Akhtar, A. (2017). DHX9 suppresses RNA processing defects originating from the Alu invasion of the human genome. Nature *544*, 115-119.
3. Athanasiadis, A., Rich, A., and Maas, S. (2004). Widespread A-to-I RNA editing of Alu-containing mRNAs in the human transcriptome. PLOS Biology *2*, e391.
4. Boukhaled, G.M., Harding, S., and Brooks, D.G. (2021). Opposing roles of type I interferons in cancer immunity. Annual Review of Pathology: Mechanisms of Disease *16*, 167-198.
5. Bowling, E.A., Wang, J.H., Gong, F., Wu, W., Neill, N.J., Kim, I.S., Tyagi, S., Orellana, M., Kurley, S.J., Dominguez-Vidaña, R., et al. (2021). Spliceosome-targeted therapies trigger an antiviral immune response in triple-negative breast cancer. Cell *184*, 384-403.e321.
6. Carpenter, S., and O'Neill, L.A.J. (2024). From periphery to center stage: 50 years of advancements in innate immunity. Cell *187*, 2030-2051.
7. Chiappinelli, K.B., Strissel, P.L., Desrichard, A., Li, H., Henke, C., Akman, B., Hein, A., Rote, N.S., Cope, L.M., Snyder, A., et al. (2015). Inhibiting DNA methylation causes an interferon response in cancer via dsRNA including endogenous retroviruses. Cell *162*, 974-986.
8. Chomiak, A.A., Tiedemann, R.L., Liu, Y., Kong, X., Cui, Y., Wiseman, A.K., Thurlow, K.E., Cornett, E.M., Topper, M.J., Baylin, S.B., and Rothbart, S.B. (2024). Select EZH2 inhibitors enhance viral mimicry effects of DNMT inhibition through a mechanism involving NFAT:AP-1 signaling. Sci Adv *10*, eadk4423.
9. Chung, H., Calis, J.J.A., Wu, X., Sun, T., Yu, Y., Sarbanes, S.L., Dao Thi, V.L., Shilvock, A.R., Hoffmann, H.H., Rosenberg, B.R., and Rice, C.M. (2018). Human ADAR1 prevents endogenous RNA from triggering translational shutdown. Cell *172*, 811-824 e814.
10. Crow, M.K., Olferiev, M., and Kirou, K.A. (2019). Type I Interferons in Autoimmune Disease. Annual Review of Pathology: Mechanisms of Disease *14*, 369-393.
11. Demaria, O., Cornen, S., Daëron, M., Morel, Y., Medzhitov, R., and Vivier, E. (2019). Harnessing innate immunity in cancer therapy. Nature *574*, 45-56.
12. Dhamdhere, M.R., Gowda, C.P., Singh, V., Liu, Z., Carruthers, N., Grant, C.N., Sharma, A., Dovat, S., Sundstrom, J.M., Wang, H.-G., and Spiegelman, V.S. (2023). IGF2BP1 regulates the cargo of extracellular vesicles and promotes neuroblastoma metastasis. Oncogene *42*, 1558-1571.
13. Elcheva, I.A., Wood, T., Chiarolanzio, K., Chim, B., Wong, M., Singh, V., Gowda, C.P., Lu, Q., Hafner, M., Dovat, S., et al. (2020). RNA-binding protein IGF2BP1 maintains leukemia stem cell properties by regulating HOXB4, MYB, and ALDH1A1. Leukemia *34*, 1354-1363.

14. Flynn, R.A., Zhang, Q.C., Spitale, R.C., Lee, B., Mumbach, M.R., and Chang, H.Y. (2016). Transcriptome-wide interrogation of RNA secondary structure in living cells with icSHAPE. Nature Protocols *11*, 273-290.
15. Gao, Y., Vasic, R., Song, Y., Teng, R., Liu, C., Gbyli, R., Biancon, G., Nelakanti, R., Lobben, K., Kudo, E., et al. (2020). m^{6}A modification prevents formation of endogenous double-stranded RNAs and deleterious innate immune responses during hematopoietic development. Immunity *52*, 1007-1021.e1008.
16. Haberman, Y., Tickle, T.L., Dexheimer, P.J., Kim, M.O., Tang, D., Karns, R., Baldassano, R.N., Noe, J.D., Rosh, J., Markowitz, J., et al. (2014). Pediatric Crohn disease patients exhibit specific ileal transcriptome and microbiome signature. J Clin Invest *124*, 3617-3633.
17. Hagemann, S., Misiak, D., Bell, J.L., Fuchs, T., Lederer, M.I., Bley, N., Hämmerle, M., Ghazy, E., Sippl, W., Schulte, J.H., and Hüttelmaier, S. (2023). IGF2BP1 induces neuroblastoma via a druggable feedforward loop with MYCN promoting 17q oncogene expression. Molecular Cancer *22*, 88.
18. Hammer, N.A., Hansen, T., Byskov, A.G., Rajpert-De Meyts, E., Grøndahl, M.L., Bredkjaer, H.E., Wewer, U.M., Christiansen, J., and Nielsen, F.C. (2005). Expression of IGF-II mRNA-binding proteins (IMPs) in gonads and testicular cancer. Reproduction *130*, 203-212.
19. Hansen, T.V.O., Hammer, N.A., Nielsen, J., Madsen, M., Dalbaeck, C., Wewer, U.M., Christiansen, J., and Nielsen, F.C. (2004). Dwarfism and impaired gut development in insulin-like growth factor II mRNA-binding protein 1-deficient mice. Molecular and Cellular Biology *24*, 4448-4464.
20. He, S., Valkov, E., Cheloufi, S., and Murn, J. (2023). The nexus between RNA-binding proteins and their effectors. Nature Reviews Genetics *24*, 276-294.
21. Hentze, M.W., Sommerkamp, P., Ravi, V., and Gebauer, F. (2025). Rethinking RNA-binding proteins: Riboregulation challenges prevailing views. Cell *188*, 4811-4827.
22. Hofer, M.J., Modesti, N., Coufal, N.G., Wang, Q., Sase, S., Miner, J.J., Vanderver, A., and Bennett, M.L. (2024). The prototypical interferonopathy: Aicardi-Goutières syndrome from bedside to bench. Immunological Reviews *327*, 83-99.
23. Hu, A., Sun, L., Lin, H., Liao, Y., Yang, H., and Mao, Y. (2024). Harnessing innate immune pathways for therapeutic advancement in cancer. Signal Transduction and Targeted Therapy *9*, 68.
24. Hu, S.B., Heraud-Farlow, J., Sun, T., Liang, Z., Goradia, A., Taylor, S., Walkley, C.R., and Li, J.B. (2023). ADAR1p150 prevents MDA5 and PKR activation via distinct mechanisms to avert fatal autoinflammation. Mol Cell *83*, 3869-3884 e3867.
25. Huang, X., Zhang, H., Guo, X., Zhu, Z., Cai, H., and Kong, X. (2018). Insulin-like growth factor 2 mRNA-binding protein 1 (IGF2BP1) in cancer. Journal of Hematology & Oncology *11*, 88.
26. Hur, S. (2019). Double-stranded RNA sensors and modulators in innate immunity. Annu Rev Immunol *37*, 349-375.
27. Hüttelmaier, S., Zenklusen, D., Lederer, M., Dictenberg, J., Lorenz, M., Meng, X., Bassell, G.J., Condeelis, J., and Singer, R.H. (2005). Spatial regulation of β-actin translation by Src-dependent phosphorylation of ZBP1. Nature *438*, 512-515.

28. Kim, E.Z., Wespiser, A.R., and Caffrey, D.R. (2016). The domain structure and distribution of Alu elements in long noncoding RNAs and mRNAs. RNA *22*, 254-264.
29. Kinker, G.S., Greenwald, A.C., Tal, R., Orlova, Z., Cuoco, M.S., McFarland, J.M., Warren, A., Rodman, C., Roth, J.A., Bender, S.A., et al. (2020). Pan-cancer single-cell RNA-seq identifies recurring programs of cellular heterogeneity. Nature Genetics *52*, 1208-1218.
30. Li, B., Zhu, L., Lu, C., Wang, C., Wang, H., Jin, H., Ma, X., Cheng, Z., Yu, C., Wang, S., et al. (2021). circNDUFB2 inhibits non-small cell lung cancer progression via destabilizing IGF2BPs and activating anti-tumor immunity. Nat Commun *12*, 295.
31. Li, H.-T., Jang, H.J., Rohena-Rivera, K., Liu, M., Gujar, H., Kulchycki, J., Zhao, S., Billet, S., Zhou, X., Weisenberger, D.J., et al. (2023). RNA mis-splicing drives viral mimicry response after DNMTi therapy in SETD2-mutant kidney cancer. Cell Reports *42*.
32. Liang, Y., Hannan, R., and Fu, Y.-X. (2021). Type I IFN Activating Type I Dendritic Cells for Antitumor Immunity. Clin. Cancer. Res.
33. Lim, Y.W., Sanz, L.A., Xu, X., Hartono, S.R., and Chédin, F. (2015). Genome-wide DNA hypomethylation and RNA:DNA hybrid accumulation in Aicardi–Goutières syndrome. eLife *4*, e08007.
34. Masson, E., Maestri, S., Bordeau, V., Cooper, D.N., Férec, C., and Chen, J.-M. (2024). *Alu* insertion-mediated dsRNA structure formation with pre-existing *Alu* elements as a disease-causing mechanism. The American Journal of Human Genetics *111*, 2176-2189.
35. Maticzka, D., Ilik, I.A., Aktas, T., Backofen, R., and Akhtar, A. (2018). uvCLAP is a fast and non-radioactive method to identify in vivo targets of RNA-binding proteins. Nat Commun *9*, 1142.
36. Morris, J.H., Knudsen, G.M., Verschueren, E., Johnson, J.R., Cimermancic, P., Greninger, A.L., and Pico, A.R. (2014). Affinity purification-mass spectrometry and network analysis to understand protein-protein interactions. Nature protocols *9*, 2539-2554.
37. Müller, S., Bley, N., Busch, B., Glaß, M., Lederer, M., Misiak, C., Fuchs, T., Wedler, A., Haase, J., Bertoldo, J.B., et al. (2020). The oncofetal RNA-binding protein IGF2BP1 is a druggable, post-transcriptional super-enhancer of E2F-driven gene expression in cancer. Nucleic Acids Research *48*, 8576-8590.
38. Müller, S., Glaß, M., Singh, A.K., Haase, J., Bley, N., Fuchs, T., Lederer, M., Dahl, A., Huang, H., Chen, J., et al. (2018). IGF2BP1 promotes SRF-dependent transcription in cancer in a m6A- and miRNA-dependent manner. Nucleic Acids Research *47*, 375-390.
39. Murayama, T., Nakayama, J., Jiang, X., Miyata, K., Morris, A.D., Cai, K.Q., Prasad, R.M., Ma, X., Efimov, A., Belani, N., et al. (2024). Targeting DHX9 triggers tumor-intrinsic interferon response and replication stress in small cell lung cancer. Cancer Discov *14*, 468-491.
40. Panthi, A., and Lynch, K.W. (2025). RNA processing in innate immunity: regulation by RNA-binding proteins. Trends in Biochemical Sciences *50*, 610-621.

41. Peng, W., Liang, J., Qian, X., Li, M., Nie, M., and Chen, B. (2025). IGF2BP1/AIFM2 axis regulates ferroptosis and glycolysis to drive hepatocellular carcinoma progression. Cellular Signalling *130*, 111660.
42. Rice, G.I., Kasher, P.R., Forte, G.M., Mannion, N.M., Greenwood, S.M., Szynkiewicz, M., Dickerson, J.E., Bhaskar, S.S., Zampini, M., Briggs, T.A., et al. (2012). Mutations in *ADAR1* cause Aicardi-Goutieres syndrome associated with a type I interferon signature. Nat Genet *44*, 1243-1248.
43. Sasaki, N., Homme, M., Murayama, T., Osaki, T., Tenma, T., An, T., Takegami, Y., Tani, T., Gedeon, P.C., Kobayashi, Y., et al. (2025). RNA sensing induced by chromosome missegregation augments anti-tumor immunity. Molecular Cell *85*, 770-786.e777.
44. Sato, T., Vries, R.G., Snippert, H.J., van de Wetering, M., Barker, N., Stange, D.E., van Es, J.H., Abo, A., Kujala, P., Peters, P.J., and Clevers, H. (2009). Single Lgr5 stem cells build crypt-villus structures in vitro without a mesenchymal niche. Nature *459*, 262-265.
45. Schonborn, J., Oberstraβ, J., Breyel, E., Tittgen, J., Schumacher, J., and Lukacs, N. (1991). Monoclonal antibodies to double-stranded RNA as probes of RNA structure in crude nucleic acid extracts. Nucleic Acids Res. *19*, 2993-3000.
46. Setti, A., Bini, G., Pellegrini, F., Maiorca, V., Proietti, G., Vrachnos, D.-M., D'Angelo, A., Armaos, A., Martone, J., Monti, M., et al. (2026). The role of low-complexity repeats in RNA–RNA interactions and a deep learning framework for duplex prediction. Nature Communications *17*, 1637.
47. Singh, V., Gowda, C.P., Singh, V., Ganapathy, A.S., Karamchandani, D.M., Eshelman, M.A., Yochum, G.S., Nighot, P., and Spiegelman, V.S. (2020). The mRNA-binding protein IGF2BP1 maintains intestinal barrier function by up-regulating occludin expression. Journal of Biological Chemistry *295*, 8602-8612.
48. Smola, M.J., Christy, T.W., Inoue, K., Nicholson, C.O., Friedersdorf, M., Keene, J.D., Lee, D.M., Calabrese, J.M., and Weeks, K.M. (2016). SHAPE reveals transcript-wide interactions, complex structural domains, and protein interactions across the Xist lncRNA in living cells. Proceedings of the National Academy of Sciences *113*, 10322-10327.
49. Stöhr, N., Köhn, M., Lederer, M., Glaß, M., Reinke, C., Singer, R.H., and Hüttelmaier, S. (2012). IGF2BP1 promotes cell migration by regulating MK5 and PTEN signaling. Genes & Development *26*, 176-189.
50. Stone, M.L., Chiappinelli, K.B., Li, H., Murphy, L.M., Travers, M.E., Topper, M.J., Mathios, D., Lim, M., Shih, I.-M., Wang, T.-L., et al. (2017). Epigenetic therapy activates type I interferon signaling in murine ovarian cancer to reduce immunosuppression and tumor burden. Proceedings of the National Academy of Sciences *114*, E10981-E10990.
51. Sun, T., Li, Q., Geisinger, J.M., Hu, S.-B., Fan, B., Su, S., Tsui, W., Guo, H., Ma, J., and Li, J.B. (2025). ADAR1 editing is necessary for only a small subset of cytosolic dsRNAs to evade MDA5-mediated autoimmunity. Nature Genetics *57*, 3101-3111.
52. Tufail, M., Jiang, C.-H., and Li, N. (2025). Immune evasion in cancer: mechanisms and cutting-edge therapeutic approaches. Signal Transduction and Targeted Therapy *10*, 227.

53. Turner, M., and Petkau, G. (2026). RNA-binding proteins and ribonucleoproteins as determinants of immunity. Nature Reviews Immunology *26*, 382-403.
54. Van Nostrand, E.L., Pratt, G.A., Shishkin, A.A., Gelboin-Burkhart, C., Fang, M.Y., Sundararaman, B., Blue, S.M., Nguyen, T.B., Surka, C., Elkins, K., et al. (2016). Robust transcriptome-wide discovery of RNA-binding protein binding sites with enhanced CLIP (eCLIP). Nat. Methods *13*, 508.
55. Wang, Y., Tan, R., and Chen, Y. (2025). Organoid culture of different intestinal segments from human and mouse. In Organoids: Models for Development and Disease, K. Turksen, ed. (Springer US), pp. 47-55.
56. Weidensdorfer, D., Stöhr, N., Baude, A., Lederer, M., Köhn, M., Schierhorn, A., Buchmeier, S., Wahle, E., and Hüttelmaier, S. (2009). Control of c-myc mRNA stability by IGF2BP1-associated cytoplasmic RNPs. RNA *15*, 104-115.
57. Xiao, P., Meng, Q., Liu, Q., Lang, Q., Yin, Z., Li, G., Li, Z., Xu, Y., Yu, Z., Geng, Q., et al. (2023). IGF2BP1-mediated N6-methyladenosine modification promotes intrahepatic cholangiocarcinoma progression. Cancer Letters *557*, 216075.
58. Xu, X., Peng, Q., Ren, Z., Han, Y., Jiang, X., Wu, Z., Tan, S., Yang, W., Oyang, L., Luo, X., et al. (2025). CircRNF13 enhances IGF2BP1 phase separation-mediated ITGB1 mRNA stabilization in an m6A-dependent manner to promote oral cancer cisplatin chemoresistance. Molecular Cancer *24*, 36.
59. Yu, M., Jo, D., Shin, W., and Han, K. (2026). The role of *Alu* elements in causing *BRCA1* structural variation and breast cancer susceptibility. Genes & Genomics *48*, 1-13.

Acknowledgements

We thank Suneng Fu and Qiang Ding for insightful comments and helpful suggestions. This project is supported by the National Natural Science Foundation of China (Grant No. 32125007 to Q.C.Z.), the Tsinghua University Initiative Scientific Research Program (Grant No. 20251080102 to Q.C.Z.), the Beijing Advanced Innovation Center for Structural Biology, the Tsinghua-Peking Joint Center for Life Sciences. This work was also supported by the Science and Technology Project of Hebei Education Department (QN2023022).

Author contributions

Q.C.Z. conceived and supervised the project. S.Z. performed all the experiments except for cancer data mining, with the help from P.W., Y.W., and L.T.. W.H., X.M., and X.Y. analyzed the cancer data. W.H., X.M., Y.A., X.H., and S.Z. analyzed all the results. S.Z. and Q.C.Z., wrote the manuscript with inputs from all authors.

Declaration of interests

The authors declare no competing interests.

Figure Legends

Figure 1. IGF2BP1 knockout robustly activates the expression of double-stranded RNA sensors in mouse intestinal organoids and different type of cancer cells.

(**A**), Heatmap showing the expression levels of interferon-stimulated genes in Huh7 cells under different conditions: WT *vs.* IGF2BP1 KO (mock_KO *vs*. mock_WT), MR766-infected WT *vs*. uninfected WT (766_WT *vs*. mock_WT), MR766-infected KO *vs*. uninfected WT (766_KO *vs*. mock_WT), and MR766-infected KO *vs*. uninfected KO (766_KO *vs*. mock_KO). Log_2(FC) values are indicated by color intensity. MR766 infection was performed at a multiplicity of infection (MOI) of 1.

(**B**), Transcriptome-wide analysis of IGF2BP1 knockout (IGF2BP1-KO) versus wild type (WT) Huh7 cells without viral infection. Upregulated genes are highlighted in red, and downregulated genes are highlighted in blue. Key interferon-stimulated genes are listed, and key dsRNA sensors (*RIG-I* and *MDA5*) are highlighted in bold. Fold change (FC) $\geqslant$ 2 and adjusted *P*-value < 0.05 were set as the cutoff for differential expression.

(**C**), Western blotting analysis of type I interferon signaling-related proteins in Huh7 WT, IGF2BP1-KO, and IGF2BP1 overexpressed (OE) cells with (Infected) or without (Mock) MR766 infection (MOI=1). GAPDH was used as sample loading control.

(**D**), Western blotting analysis of RIG-I in HeLa (left) and HEK293 (right) IGF2BP1 knockout cells. WT, wild-type cells; KO1, KO2, independent IGF2BP1 knockout cell clones. GAPDH was used a sample loading control.

(**E**), Rescue experiment verifying RIG-I protein levels in IGF2BP1 knockout cells with IGF2BP1 re-expression. The overexpression vector pLVX-IGF2BP1 or pLVX-GFP (control) was

transfected into IGF2BP1 knockout cells. WT, Huh7 wild-type cells. GAPDH was used as sample loading control.

(**F**), Relative MDA5 mRNA expression levels in Huh7 WT, IGF2BP1-KO, and IGF2BP1 rescue (KO+IGF2BP1) cells. Expression levels were normalized to those in WT cells. Data are presented as mean ± SD from 3 independent biological replicates.

(**G**), Western blotting analysis of RIG-I, MDA5, and PKR in wild-type (WT) and IGF2BP1-knocked down mouse intestinal organoids. NC, scrambled shRNA; sh-1, sh-2, short hairpin RNAs targeting to *IGF2BP1*. GAPDH was used as sample loading control for western blotting.

(**H**), Type I interferon levels in Huh7 wild-type (WT), IGF2BP1 knockout (IGF2BP1-KO), IGF2BP1 rescue (KO+IGF2BP1), and peptidylprolyl isomerase A (PPIA) knockdown (shPPIA) cells. The shPPIA cells were used as background control for interferon measurement in gene-manipulation cells. Data are presented as mean ± SD from 3 independent biological replicates.

Figure 2. IGF2BP1 knockout suppresses proliferation of cancer cells and drives viral mimicry responses in cells.

(**A**, **B**) Effect of IGF2BP1 depletion on the proliferation of Huh7 (**A**) and Caco-2 (**B**) cells. WT, wild-type cells; shNC, scramble short hairpin RNA (negative control); shIGF2BP1, short hairpin RNA targeting IGF2BP1; shPPIA, short hairpin RNA targeting PPIA (negative control for gene knockdown-associated growth effects); IGF2BP1-KO, IGF2BP1 knockout cells; KO+IGF2BP1, IGF2BP1 re-expression in IGF2BP1-KO cells. IFNβ: cells cultured in medium supplemented with interferon β. Cell proliferation was assessed via CCK-8 assay at 0, 24, 48, and 72 h. Data are shown as Mean ± SEM.

(**C**), Differentially expressed genes in WT Huh7 cells infected with Zika virus strain MR766 (766_WT) versus uninfected WT cells (mock_WT).

(**D**), Transcriptome comparison between uninfected IGF2BP1 KO cells (mock_KO) and Zika virus MR766-infected IGF2BP1 KO cells (766_KO).

(**E**), Gene Ontology (GO) functional enrichment analysis of up-regulated genes in IGF2BP1-KO Huh7 cells (left) and MR766-infected WT cells (right). The top 10 enriched terms are shown.

Figure 3. The dsRNAs accumulated in IGF2BP1 knockout cells are transferable.

(**A**), Immunofluorescence analysis of cytosolic dsRNA in Huh7 wild-type (WT), IGF2BP1 knockout (KO), and IGF2BP1 re-expression (KO+IGF2BP1) cells using the dsRNA-specific J2 antibody (green). Cell nuclei were counterstained with DAPI (blue). Scale bar, 10 μm.

(**B**), Dot-blot analysis of cellular dsRNA using the J2 antibody. Total RNAs were extracted from Huh7 WT, IGF2BP1 KO, and KO+IGF2BP1 cells, and serial dilutions of total RNA were loaded onto a nitrocellulose membrane for detection.

(**C**), Changes in RNA secondary structure at IGF2BP1-binding regions in IGF2BP1 KO Huh7 cells. RNA regions were classified as IGF2BP1-bound (uvCLAP identified) or unbound. The violin plot shows the absolute value of SHAPE score differences between the two groups, reflecting structural changes. ***$P \leqslant 0.001$; Student's *t*-test.

(**D**), Transcriptome-wide RNA secondary structure analysis in Huh7 WT and IGF2BP1-KO cells. The icSHAPE was performed to quantify RNA secondary structure. Higher SHAPE score values indicate regions with a higher propensity to adopt single-stranded conformations, while lower values indicate regions with a greater propensity for double-stranded conformations. The scatter

844 plot shows pairwise comparison of SHAPE scores for all transcripts between WT and IGF2BP1-
845 KO cells.
846 (**E**), Western blotting analysis of RIG-I in HeLa cells transfected with gradient doses of dsRNA
847 purified using J2 antibody from Huh7 IGF2BP1 KO cells. Lipo, Lipofectamine 2000 alone; Luc
848 RNA, *in vitro*-transcribed luciferase RNA; J2-RNA, RNA purified via J2 antibody-based
849 immunoprecipitation from Huh7 IGF2BP1-KO cells (50 ng, 100 ng, 200 ng per transfection).
850 GAPDH was used as sample loading control.
851 (**F**), Enrichment analysis of cytosolic dsRNA in Huh7 IGF2BP1 KO cells. The dsRNA
852 enrichment efficiency quantified from two aspects: the ratio of RNA abundance in J2 antibody
853 immunoprecipitates to input samples (dsRIP/INPUT) in WT and KO cells; and the ratio of J2-
854 immunoprecipitated RNA in KO cells to that in WT cells (dsRIP *vs*. ctrl).
855 (**G**), Overlap between dsRNAs (pulled down by J2 antibody in dsRIP) and IGF2BP1-bound
856 transcripts (identified by uvCLAP) in Huh7 cells.
857 (**H**), Genome browser tracks showing dsRIP-seq signals of representative IGF2BP1 target
858 transcripts (*BZW1*, *SSR3*, *MREG*, *TMX3*) in Huh7 WT and IGF2BP1-KO cells. Sequencing reads
859 were mapped to the gene body of each indicated transcript, with gene structure annotated below.
860 The y-axis represents normalized read counts (reads per million reads, RPM).
861 (**I**), RNA secondary structure reconstruction of the *BZW1* transcript based on icSHAPE-derived
862 SHAPE scores in Huh7 WT and IGF2BP1-KO cells. Higher SHAPE scores (red) indicate a
863 greater propensity for single-stranded conformations in RNA.
864

Figure 4. IGF2BP1 preferentially binds *Alu* element containing transcripts.

(**A**), IGF2BP1 RNA-binding characteristics. Motif enrichment analysis of IGF2BP1-binding sites identified from uvCLAP (Huh7 cells) and integrated eCLIP datasets from HepG2 and K562 cells (Van Nostrand *et al.*, 2020). The top 4 significantly enriched motifs are displayed (top). Bottom: distribution of IGF2BP1-binding density across different RNA regions based on uvCLAP and eCLIP data.

(**B**), Classification of IGF2BP1-binding RNA species. The pie chart shows the percentage of different RNA types (mRNA, snoRNA, lincRNA etc.) among IGF2BP1-binding targets identified via uvCLAP in Huh7 cells.

(**C**), Gene Ontology (GO) enrichment analysis of IGF2BP1-binding RNAs. Shown are GO terms with significant enrichment (adjusted $p < 0.01$). Target RNAs were identified via uvCLAP in Huh7 cells, and background reference was the whole Huh7 mRNA transcriptome.

(**D**), Repeat element enrichment in IGF2BP1-bound transcripts. The stacked bar chart shows the percentage of different repeat element types (*e.g.*, *Alu*, simple repeats) in IGF2BP1-bound transcripts identified by uvCLAP. Binding targets of PTBP1 and TRA2A were retrieved from published eCLIP datasets (HepG2 and K562 cells; Van Nostrand et al., 2020).

Figure 5. IGF2BP1 physically cooperated with ADAR1 and DHX9 to restrain accumulation of cellular dsRNA.

(**A**), Identification of IGF2BP1-associated proteins via affinity purification-tandem mass spectrometry (AP-MS). Scatter plot showing the correlation of protein abundance between two independent biological replicates. Pearson correlation coefficient (r) is indicated.

887 (**B**), Validation of the physical interaction between IGF2BP1 and DHX9 and ADAR1 was
888 performed via co-immunoprecipitation (co-IP). Co-IP was performed using an anti-IGF2BP1
889 antibody (IP) in Huh7 cell lysates, and co-purified DHX9 and ADAR1 were detected by Western
890 blotting (IB). IgG was used as a negative control for non-specific precipitation. A parallel co-IP
891 assay was performed in RNase A-treated cell lysates (IGF2BP1+RNase A) to assess RNA
892 dependence of the interactions. GAPDH was used as sample loading and non-specific
893 precipitation control.
894 (**C**), ADAR1-mediated A-to-I editing efficiency around IGF2BP1-binding sites. The average A-
895 to-I editing ratios of IGF2BP1-bound transcripts were quantified in 100nt bins spanning 1,000nt
896 upstream and downstream of IGF2BP1-binding sites. Editing ratios were compared between
897 Huh7 wild-type (WT) and IGF2BP1 knockout (KO) cells. Data are presented as mean ± SD. *, $P \leq 0.05$; **, $P \leq 0.01$; ***, $P \leq 0.001$; Student's *t*-test.
899 (**D**), Immunofluorescence analysis of cellular dsRNA in gene-manipulated Huh7 cells. Cytosolic
900 dsRNA was detected using the dsRNA-specific J2 antibody (green) in ADAR1 knockdown
901 (shADAR1), DHX9 knockdown (shDHX9), and PPIA knockdown (shPPIA) cells. shPPIA cells
902 served as a background control for gene manipulation. Cell nuclei were counterstained with
903 DAPI (blue). Scale bar, 10 μm.
904

905 **Figure 6. IGF2BP1 overexpression is associated with suppressed innate immune activation**
906 **and poor clinical outcomes in human cancers.**

907 (**A**), Expression levels (transcripts per million, TPM) of *IGF2BP1* in patients with colon
908 adenocarcinoma. Transcriptome data of colon adenocarcinoma patients were retrieved from The
909 Cancer Genome Atlas (TCGA) colon adenocarcinoma (COAD) dataset. IGF2BP1 expression

was compared between primary tumor tissues and adjacent normal para-carcinoma tissues. Box plots represent the 5th–95th percentiles, with horizontal lines indicating medians. ***, $P \leq 0.001$; Wilcoxon rank-sum test.

(**B**), Kaplan–Meier survival analysis comparing overall survival between patients with high (yellow) and low (blue) *IGF2BP1* expression. $p = 0.022$ (log-rank test).

(**C**), Expression of interferon-stimulated genes (ISGs) across eight cancer types, including digestive system malignancies (colon carcinoma, COAD; hepatocellular carcinoma, HCC), respiratory system tumors (lung adenocarcinoma, LUAD; lung squamous cell carcinoma, LUSC), reproductive system cancers (breast cancer, BRCA; uterine carcinosarcoma, UCS), head and neck cancer (HNSC), and skin cutaneous melanoma (SKCM), comparing tumors with high versus low IGF2BP1 expression. High IGF2BP1 expression is consistently associated with diminished ISG expression. ***, $P < 0.001$; Wilcoxon rank-sum test.

(**D**, **E**) Expression levels (TPM) of *RIG-I* and *MDA5* in colon adenocarcinoma patients stratified by IGF2BP1 expression. TCGA COAD dataset was used, and patients were divided into high IGF2BP1 (top 33%) and low IGF2BP1 (bottom 33%) groups based on *IGF2BP1* transcript levels. Box plots represent the 5th–95th percentiles, with horizontal lines indicating medians. $P \leq 0.001$; Wilcoxon rank-sum test.

Figure 7. Schematic model of the IGF2BP1-ADAR-DHX9 axis in regulating endogenous dsRNA-stimulated innate immunity.

IGF2BP1 selectively binds dsRNA-prone transcripts via the "CACA" motif. ADAR1 mediates A-to-I editing to disrupt dsRNA formation, while DHX9 unwinds existing dsRNA structures.

Loss of any component of the complex leads to dsRNA accumulation and innate immune activation.

Supplementary Figures

Fig. S1 Loss of IGF2BP1 leads to induction of immunogenic double-stranded RNAs in human cells.

(**A**), Western blot analysis of IGF2BP1 protein expression in Huh7 cells. WT, Huh7 wild-type cells; IGF2BP1-KO, IGF2BP1 knockout cells; OE, IGF2BP1-overexpressing cells. GAPDH was used as sample loading control.

(**B**), Immunofluorescence assay (IFA) of dsRNA in HeLa cells. WT, HeLa wild-type cells; IGF2BP1-KO, HeLa IGF2BP1 knockout cells. The dsRNA was detected with the J2 antibody (green), and nuclei were stained with DAPI (blue). Scale bar, 10 μm.

(**C**), Correlation of transcript abundance (RPKM) between replications of icSHAPE sequencing. RNA-seq (DMSO) in Huh7 wild-type (WT) and IGF2BP1 knockout (IGF2BP1-KO) cells was used to compare transcript abundance (RPKM) between two replications from icSHAPE sequencing data.

(**D**), Receiver-operating characteristic (ROC) curve for evaluating the performance of RNA secondary structure reconstruction using icSHAPE data. WT, icSHAPE in Huh7 wild-type cells; KO, icSHAPE in IGF2BP1 knockout cells (IGF2BP1-KO).

(**E**), Cross-validation of RNA secondary structure reconstruction performance. Human 18S rRNA (with a well-characterized secondary structure, PDB entry: 4V6X) was used for cross-validation through mapping SHAPE scores to individual nucleotides. SHAPE scores are represented by different colors, with higher scores (in red) indicating more accessible single-stranded regions of RNA.

(**F**), Western blotting analysis of dsRNA sensors (RIG-I, MDA5, PKR) in Huh7 wild-type (WT) and IGF2BP1-overexpressed (OE) cells transfected with RNAs from different sources. Lipo,

957 Lipofectamine 2000 alone (transfection reagent control); Luc RNA, *in vitro*-transcribed
958 luciferase RNA (non-immunogenic RNA control); WT RNA, RNA purified from Huh7 WT cells;
959 KO RNA, RNA purified from Huh7 IGF2BP1 knockout (KO) cells. Approximately 200 ng of
960 RNA was transfected. GAPDH was used as sample loading control.
961

962 **Fig. S2 Elevated *IGF2BP1* expression in multiple human cancers correlates with adverse**
963 **clinical outcomes.**

964 (**A**), IGF2BP1 upregulation across various cancer types. Red dots denote malignancies with
965 significantly increased IGF2BP1 mRNA expression ($P < 0.05$, Wilcoxon rank-sum test), and
966 gray dots indicate cancers with no significant change in IGF2BP1 levels. BLCA, bladder cancer;
967 BRCA, breast cancer; COAD, colon carcinoma; ESCA, esophageal carcinoma; HNSC, head and
968 neck cancer; HCC, hepatocellular carcinoma; LUAD, lung adenocarcinoma; LUSC, lung
969 squamous cell carcinoma; OV, ovarian cancer; READ, rectal adenocarcinoma; SKCM, skin
970 cutaneous melanoma; STAD, stomach adenocarcinoma; UCEC, uterine corpus endometrial
971 carcinoma; KICH, kidney chromophobe carcinoma; KIRP, kidney papillary cell carcinoma;
972 KIRC, kidney clear cell carcinoma; PRAD, prostate adenocarcinoma, THCA, thyroid carcinoma.
973 (**B-J**), IGF2BP1 mRNA levels across various human cancers. *IGF2BP1* expression was
974 compared between cancer and matched normal or para-carcinoma tissues. TPM, transcripts per
975 kilobase million. Box plots represent the 5th–95th percentiles, with horizontal lines indicating
976 medians. ***, $P \leq 0.001$; Wilcoxon rank-sum test.
977 (**K-N**), Kaplan–Meier survival curves for overall survival stratified by IGF2BP1 expression.
978 Patients with high *IGF2BP1* expression are shown in yellow, and those with low expression in
979 blue. Analyses were performed across four cancer types: stomach adenocarcinoma (STAD), lung

adenocarcinoma (LUAD), breast invasive carcinoma (BRCA), and uterine corpus endometrial carcinoma (UCEC). The *p* values were calculated using the log-rank test and presented in the corresponding panels.

Fig. S3 Correlation between IGF2BP1 expression and innate immunity-associated genes across diverse human cancers.

(**A-D**), Expression of interferon stimulated genes in patients with colon adenocarcinoma (**A**), hepatocellular carcinoma (**B**), lung adenocarcinoma (**C**), and stomach cancer (**D**). TCGA cancer dataset was used, and patients were divided into high IGF2BP1 (top 33%) and low IGF2BP1 (bottom 33%) groups based on *IGF2BP1* transcript levels. Box plots represent the 5th–95th percentiles, with horizontal lines indicating medians. *, $P \leq 0.05$; **, $P \leq 0.01$; ***, $P \leq 0.001$; Wilcoxon rank-sum test.

Fig. S4 Correlation between IGF2BP1 expression and double-stranded RNA sensors in human cancers and inflammatory bowel diseases.

(**A-B**), Expression of dsRNA sensor coding genes *RIG-1* and *MDA5* in patients with ovarian cancer (**A**), or head and neck cancer (**B**). Patients were divided into high IGF2BP1 (top 33%) and low IGF2BP1 (bottom 33%) groups based on *IGF2BP1* transcript levels. Box plots represent the 5th–95th percentiles, with horizontal lines indicating medians. *, $P \leq 0.05$; **, $P \leq 0.01$; ***, $P \leq 0.001$; Wilcoxon rank-sum test.

(**C**), Expression levels of *IGF2BP1*, *IGF2BP2*, and *IGF2BP3* in pediatric patients with ileal Crohn's disease (CD) or ulcerative colitis (UC). Transcriptome data from patients with

inflammatory bowel disease (GEO series accession number GSE57945; Haberman et al, 2014) were re-analyzed to assess the expression of IGF2BP family members. Box plots represent the 5th–95th percentiles, with horizontal lines indicating medians. *, $P \leq 0.05$; **, $P \leq 0.01$; ***, $P \leq 0.001$; n.s., not significant; Wilcoxon rank-sum test.

(**D**), Expression of dsRNA sensor coding genes *RIG-1* and *MDA5* in patients with Corhn's disease or ulcerative colitis. Box plots represent the 5th–95th percentiles, with horizontal lines indicating medians. **, $P \leq 0.01$; Wilcoxon rank-sum test.

Fig. 1

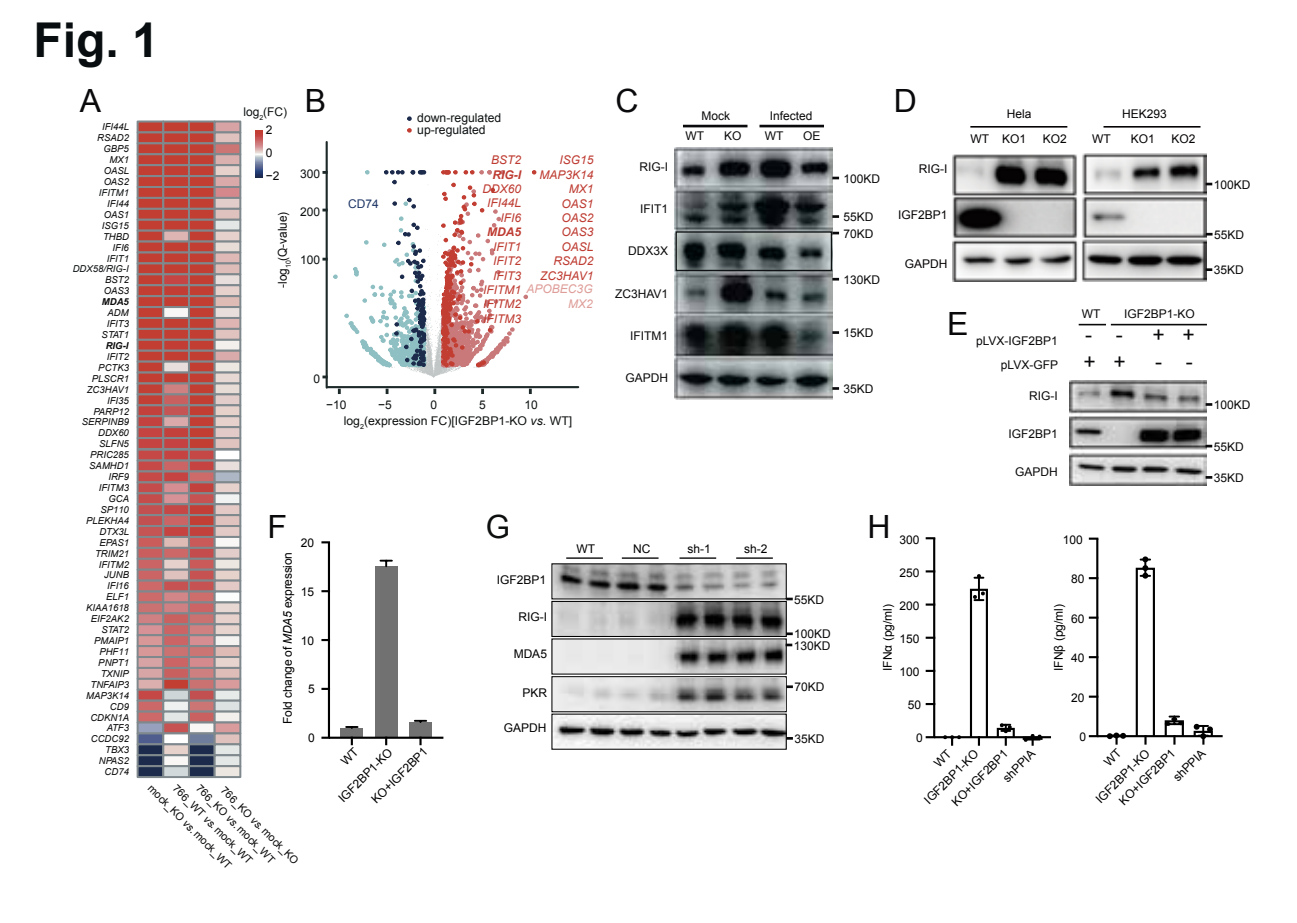
A
log2(FC)
2
0
−2
IFI44L
RSAD2
GBP5
MX1
OASL
OAS2
IFITM1
IFI44
OAS1
ISG15
THBD
IFI6
IFIT1
DDX58/RIG-I
BST2
OAS3
MDA5
ADM
IFIT3
STAT1
RIG-I
IFIT2
PCTK3
PLSCR1
ZC3HAV1
IFI35
PARP12
SERPINB9
DDX60
SLFN5
PRIC285
SAMHD1
IRF9
IFITM3
GCA
SP110
PLEKHA4
DTX3L
EPAS1
TRIM21
IFITM2
JUNB
IFI16
ELF1
KIAA1618
EIF2AK2
STAT2
PMAIP1
PHF11
PNPT1
TXNIP
TNFAIP3
MAP3K14
CD9
CDKN1A
ATF3
CCDC92
TBX3
NPAS2
CD74
mock_KO vs.mock_WT
766_WT vs. mock_WT
766_KO vs. mock_WT
766_KO vs. mock_KO
B
down-regulated
up-regulated
-log10(Q-value)
300
200
100
0
CD74
BST2
RIG-I
DDX60
IFI44L
IFI6
MDA5
IFIT1
IFIT2
IFIT3
IFITM1
IFITM2
IFITM3
ISG15
MAP3K14
MX1
OAS1
OAS2
OAS3
OASL
RSAD2
ZC3HAV1
APOBEC3G
MX2
−10
−5
0
5
10
log2(expression FC)[IGF2BP1-KO vs. WT]
C
Mock
Infected
WT
KO
WT
OE
RIG-I
IFIT1
DDX3X
ZC3HAV1
IFITM1
GAPDH
100KD
55KD
70KD
130KD
15KD
35KD
D
Hela
HEK293
WT
KO1
KO2
WT
KO1
KO2
RIG-I
IGF2BP1
GAPDH
100KD
55KD
35KD
E
WT
IGF2BP1-KO
pLVX-IGF2BP1
pLVX-GFP
RIG-I
IGF2BP1
GAPDH
100KD
55KD
35KD
F
Fold change of MDA5 expression
20
15
10
5
0
WT
IGF2BP1-KO
KO+IGF2BP1
G
WT
NC
sh-1
sh-2
IGF2BP1
RIG-I
MDA5
PKR
GAPDH
55KD
100KD
130KD
70KD
35KD
H
IFNα (pg/ml)
300
250
200
150
100
50
0
IFNβ (pg/ml)
100
80
60
40
20
0
WT
IGF2BP1-KO
KO+IGF2BP1
shPPIA

Fig. 2

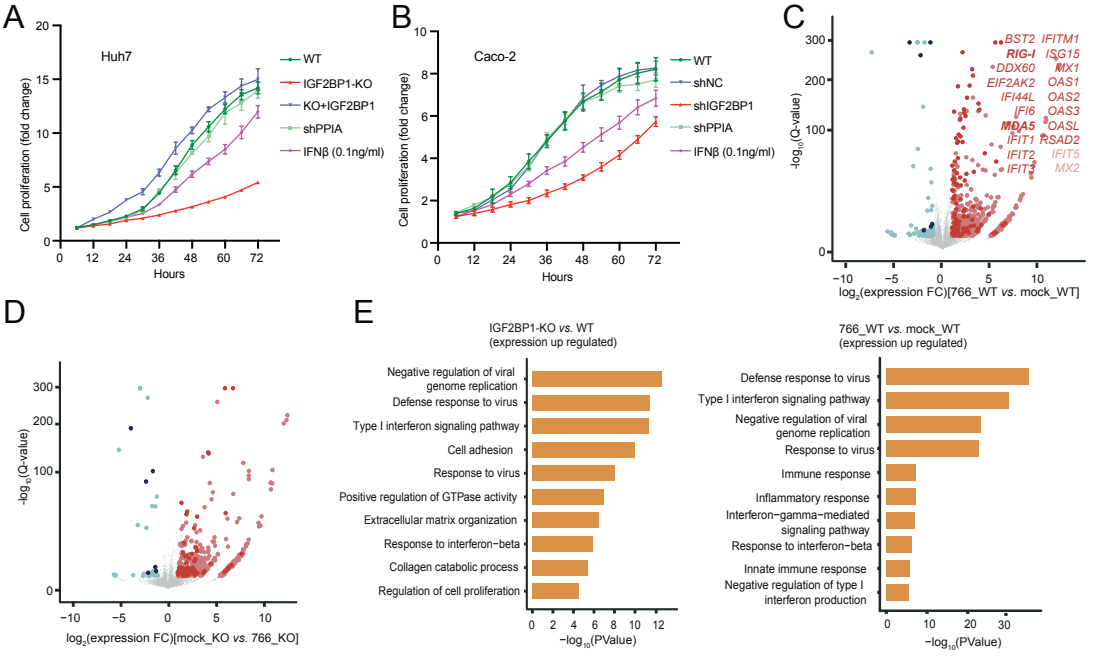
A
Huh7
WT
IGF2BP1-KO
KO+IGF2BP1
shPPIA
IFNβ (0.1ng/ml)
Cell proliferation (fold change)
Hours
B
Caco-2
WT
shNC
shIGF2BP1
shPPIA
IFNβ (0.1ng/ml)
Cell proliferation (fold change)
Hours
C
BST2
IFITM1
RIG-I
ISG15
DDX60
MX1
EIF2AK2
OAS1
IFI44L
OAS2
IFI6
OAS3
MDA5
OASL
IFIT1
RSAD2
IFIT2
IFIT5
IFIT3
MX2
-log10(Q-value)
log2(expression FC)[766_WT vs. mock_WT]
D
-log10(Q-value)
log2(expression FC)[mock_KO vs. 766_KO]
E
IGF2BP1-KO vs. WT
(expression up regulated)
Negative regulation of viral genome replication
Defense response to virus
Type I interferon signaling pathway
Cell adhesion
Response to virus
Positive regulation of GTPase activity
Extracellular matrix organization
Response to interferon−beta
Collagen catabolic process
Regulation of cell proliferation
−log10(PValue)
766_WT vs. mock_WT
(expression up regulated)
Defense response to virus
Type I interferon signaling pathway
Negative regulation of viral genome replication
Response to virus
Immune response
Inflammatory response
Interferon−gamma−mediated signaling pathway
Response to interferon−beta
Innate immune response
Negative regulation of type I interferon production
−log10(PValue)

Fig. 3

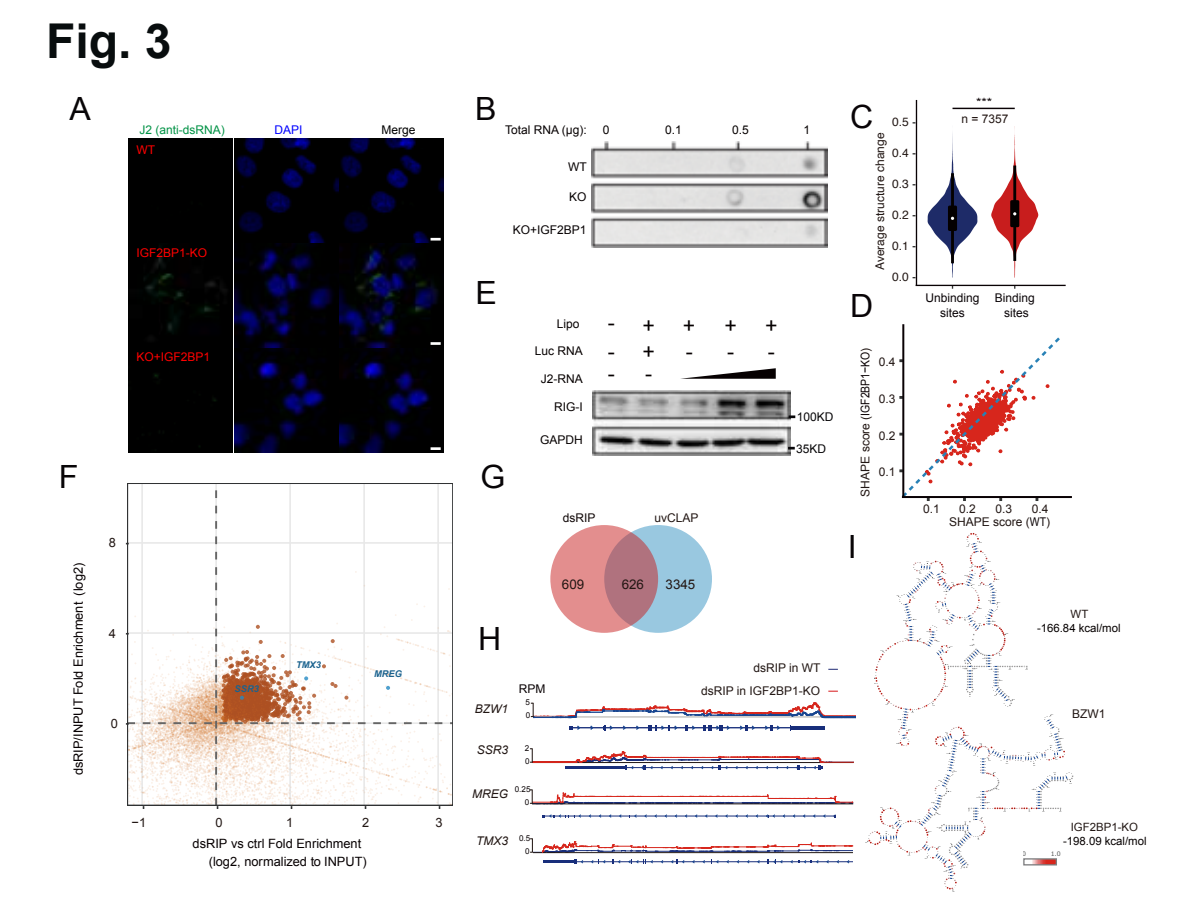
A
J2 (anti-dsRNA)
DAPI
Merge
WT
IGF2BP1-KO
KO+IGF2BP1
B
Total RNA (μg): 0 0.1 0.5 1
WT
KO
KO+IGF2BP1
C
***
n = 7357
Average structure change
Unbinding sites
Binding sites
D
SHAPE score (IGF2BP1−KO)
SHAPE score (WT)
E
Lipo
Luc RNA
J2-RNA
RIG-I
GAPDH
100KD
35KD
F
dsRIP/INPUT Fold Enrichment (log2)
dsRIP vs ctrl Fold Enrichment
(log2, normalized to INPUT)
TMX3
MREG
SSR3
G
dsRIP
uvCLAP
609
626
3345
H
RPM
dsRIP in WT
dsRIP in IGF2BP1-KO
BZW1
SSR3
MREG
TMX3
I
WT
-166.84 kcal/mol
BZW1
IGF2BP1-KO
-198.09 kcal/mol

Fig. 4

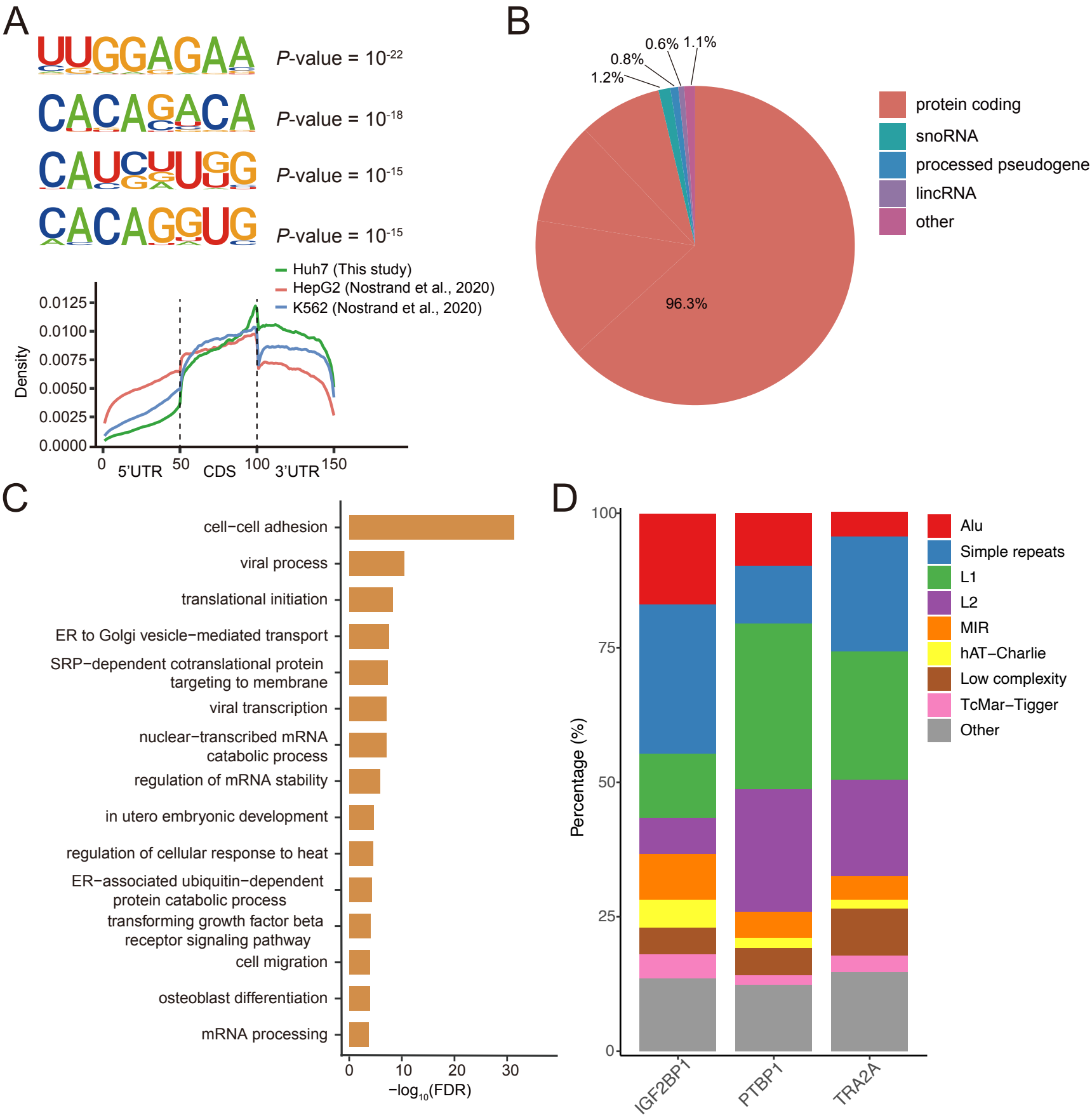
A
P-value = 10-22
P-value = 10-18
P-value = 10-15
P-value = 10-15
Huh7 (This study)
HepG2 (Nostrand et al., 2020)
K562 (Nostrand et al., 2020)
Density
0.0125
0.0100
0.0075
0.0050
0.0025
0.0000
0
5'UTR
50
CDS
100
3'UTR
150
B
0.6%
1.1%
0.8%
1.2%
96.3%
protein coding
snoRNA
processed pseudogene
lincRNA
other
C
cell−cell adhesion
viral process
translational initiation
ER to Golgi vesicle−mediated transport
SRP−dependent cotranslational protein targeting to membrane
viral transcription
nuclear−transcribed mRNA catabolic process
regulation of mRNA stability
in utero embryonic development
regulation of cellular response to heat
ER−associated ubiquitin−dependent protein catabolic process
transforming growth factor beta receptor signaling pathway
cell migration
osteoblast differentiation
mRNA processing
0
10
20
30
−log10(FDR)
D
Percentage (%)
100
75
50
25
0
IGF2BP1
PTBP1
TRA2A
Alu
Simple repeats
L1
L2
MIR
hAT−Charlie
Low complexity
TcMar−Tigger
Other

Fig. 5

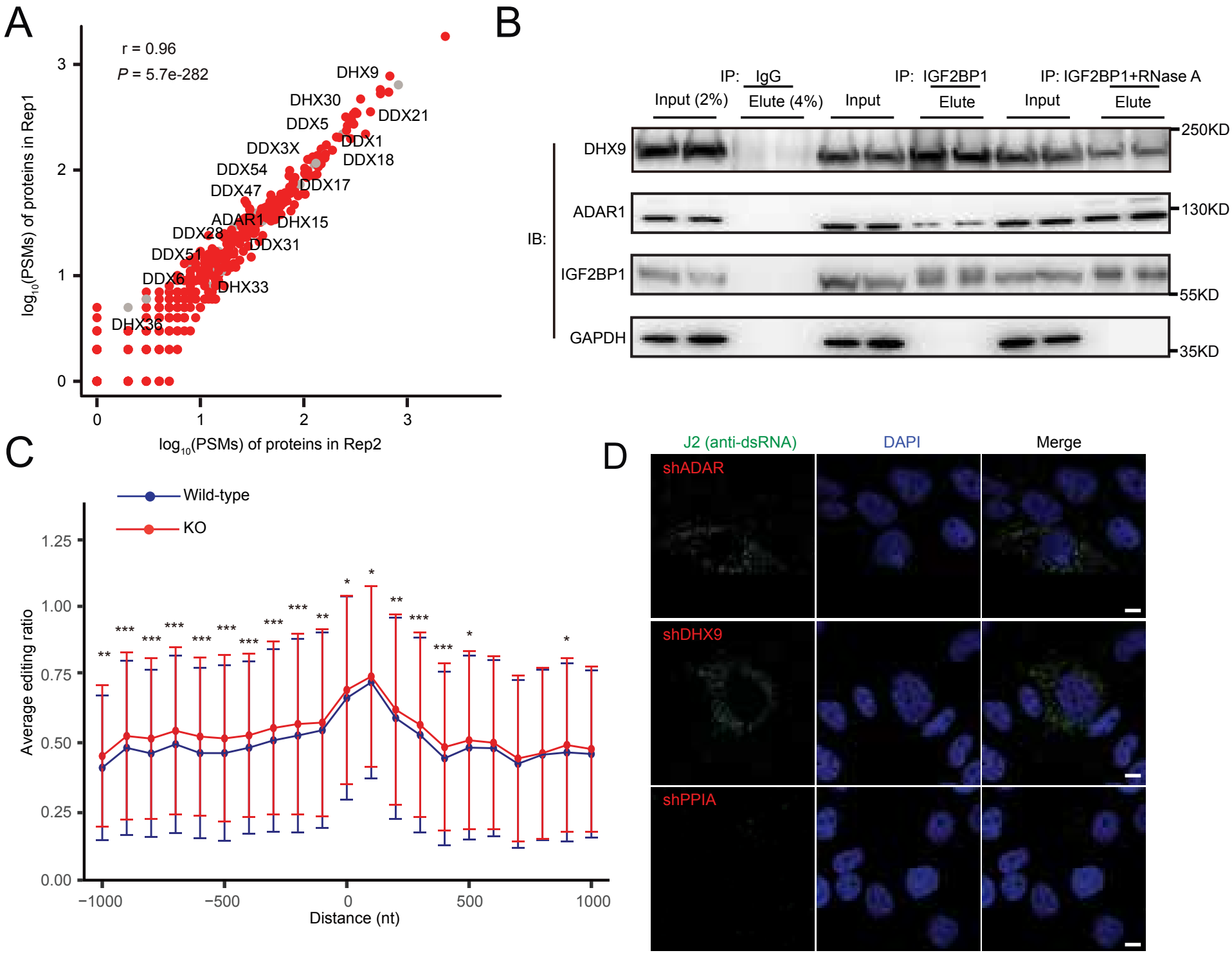
A
r = 0.96
P = 5.7e-282
DHX9
DHX30
DDX21
DDX5
DDX1
DDX3X
DDX18
DDX54
DDX17
DDX47
ADAR1
DHX15
DDX28
DDX31
DDX51
DDX6
DHX33
DHX36
log10(PSMs) of proteins in Rep1
log10(PSMs) of proteins in Rep2
B
IP: IgG
IP: IGF2BP1
IP: IGF2BP1+RNase A
Input (2%)
Elute (4%)
Input
Elute
Input
Elute
IB:
DHX9
ADAR1
IGF2BP1
GAPDH
250KD
130KD
55KD
35KD
C
Wild-type
KO
Average editing ratio
Distance (nt)
D
J2 (anti-dsRNA)
DAPI
Merge
shADAR
shDHX9
shPPIA

Fig. 6

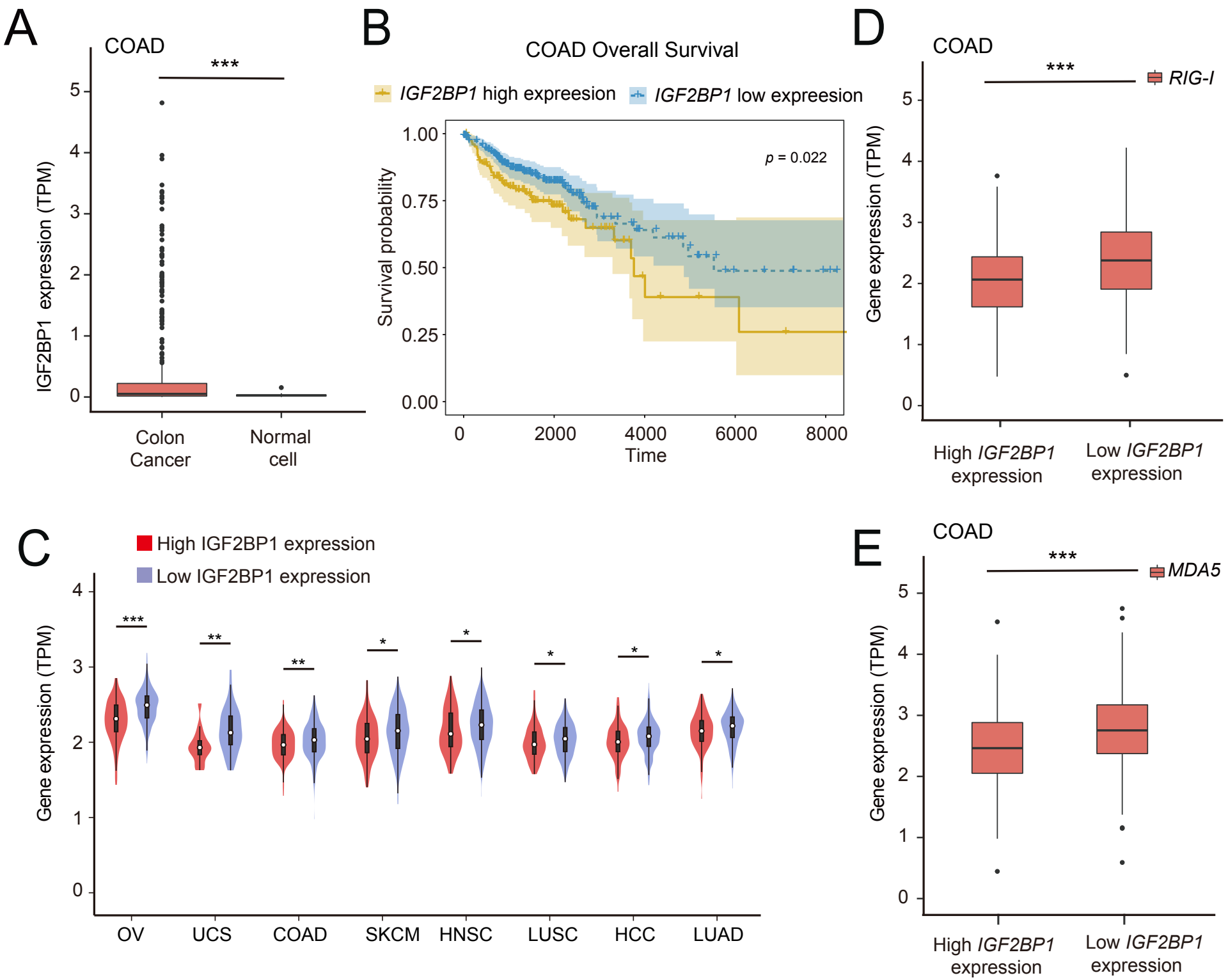
A
COAD
***
IGF2BP1 expression (TPM)
0
1
2
3
4
5
Colon Cancer
Normal cell
B
COAD Overall Survival
IGF2BP1 high expreesion
IGF2BP1 low expreesion
p = 0.022
Survival probability
0.00
0.25
0.50
0.75
1.00
0
2000
4000
6000
8000
Time
D
COAD
***
RIG-I
Gene expression (TPM)
0
1
2
3
4
5
High IGF2BP1 expression
Low IGF2BP1 expression
C
High IGF2BP1 expression
Low IGF2BP1 expression
Gene expression (TPM)
0
1
2
3
4
***
**
**
*
*
*
*
*
OV
UCS
COAD
SKCM
HNSC
LUSC
HCC
LUAD
E
COAD
***
MDA5
Gene expression (TPM)
0
1
2
3
4
5
High IGF2BP1 expression
Low IGF2BP1 expression

Fig. 7

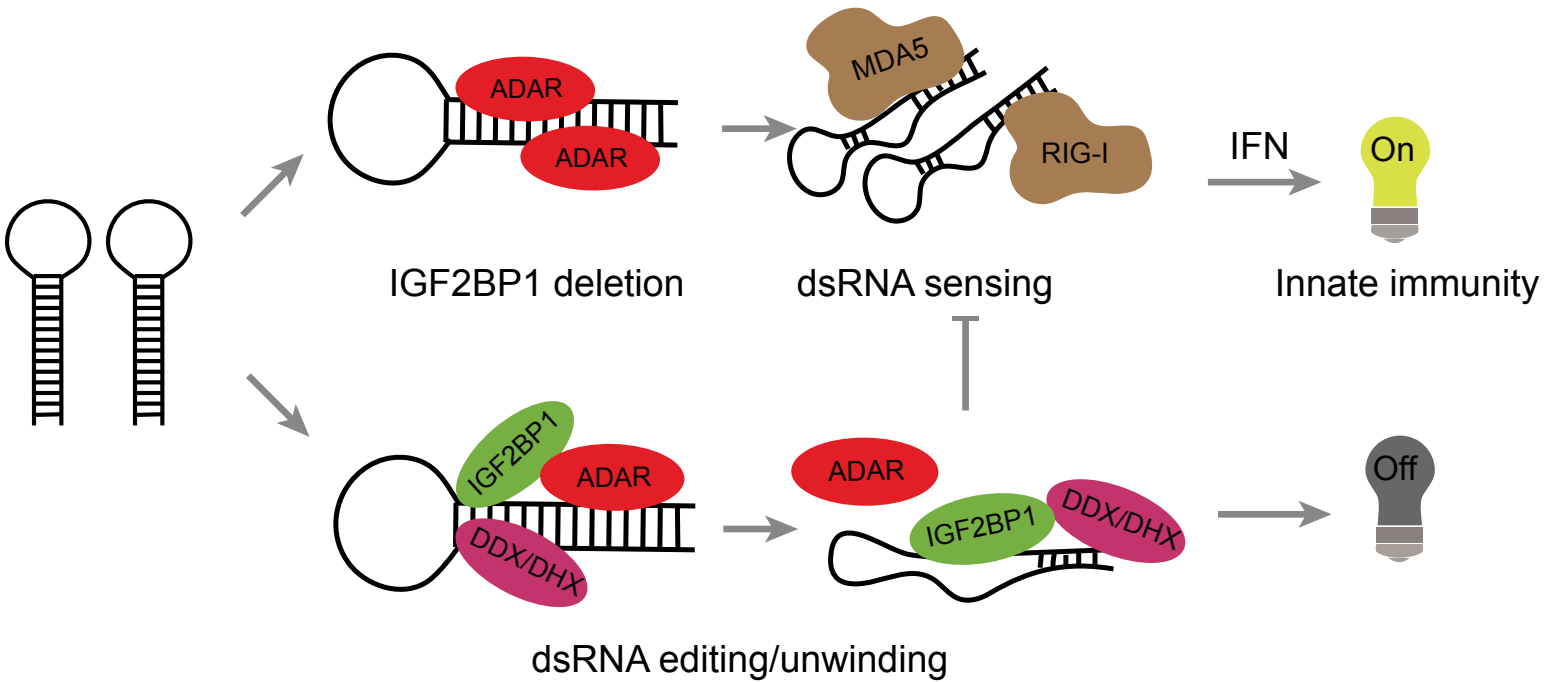
ADAR
ADAR
MDA5
RIG-I
IFN
On
IGF2BP1 deletion
dsRNA sensing
Innate immunity
IGF2BP1
ADAR
DDX/DHX
ADAR
IGF2BP1
DDX/DHX
Off
dsRNA editing/unwinding

Fig. S1

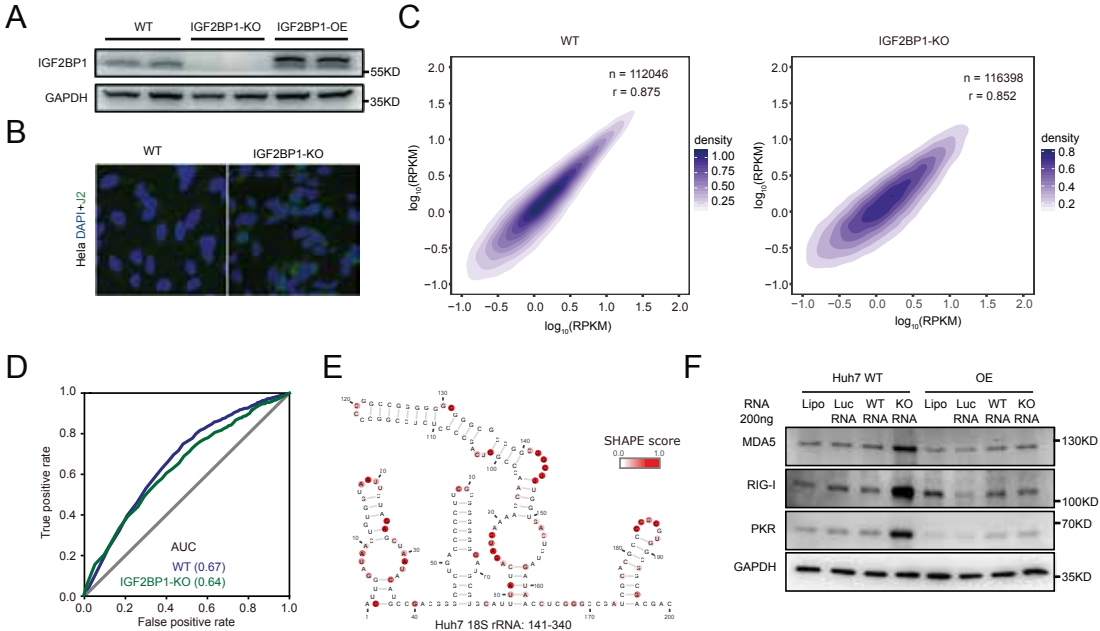
A
WT
IGF2BP1-KO
IGF2BP1-OE
IGF2BP1
55KD
GAPDH
35KD
B
WT
IGF2BP1-KO
Hela DAPI+/2
C
WT
n = 112046
r = 0.875
IGF2BP1-KO
n = 116398
r = 0.852
density
log10(RPKM)
D
True positive rate
False positive rate
AUC
WT (0.67)
IGF2BP1-KO (0.64)
E
SHAPE score
Huh7 18S rRNA: 141-340
F
Huh7 WT
OE
RNA 200ng
Lipo
Luc RNA
WT RNA
KO RNA
MDA5
RIG-I
PKR
GAPDH
130KD
100KD
70KD
35KD

Fig. S2

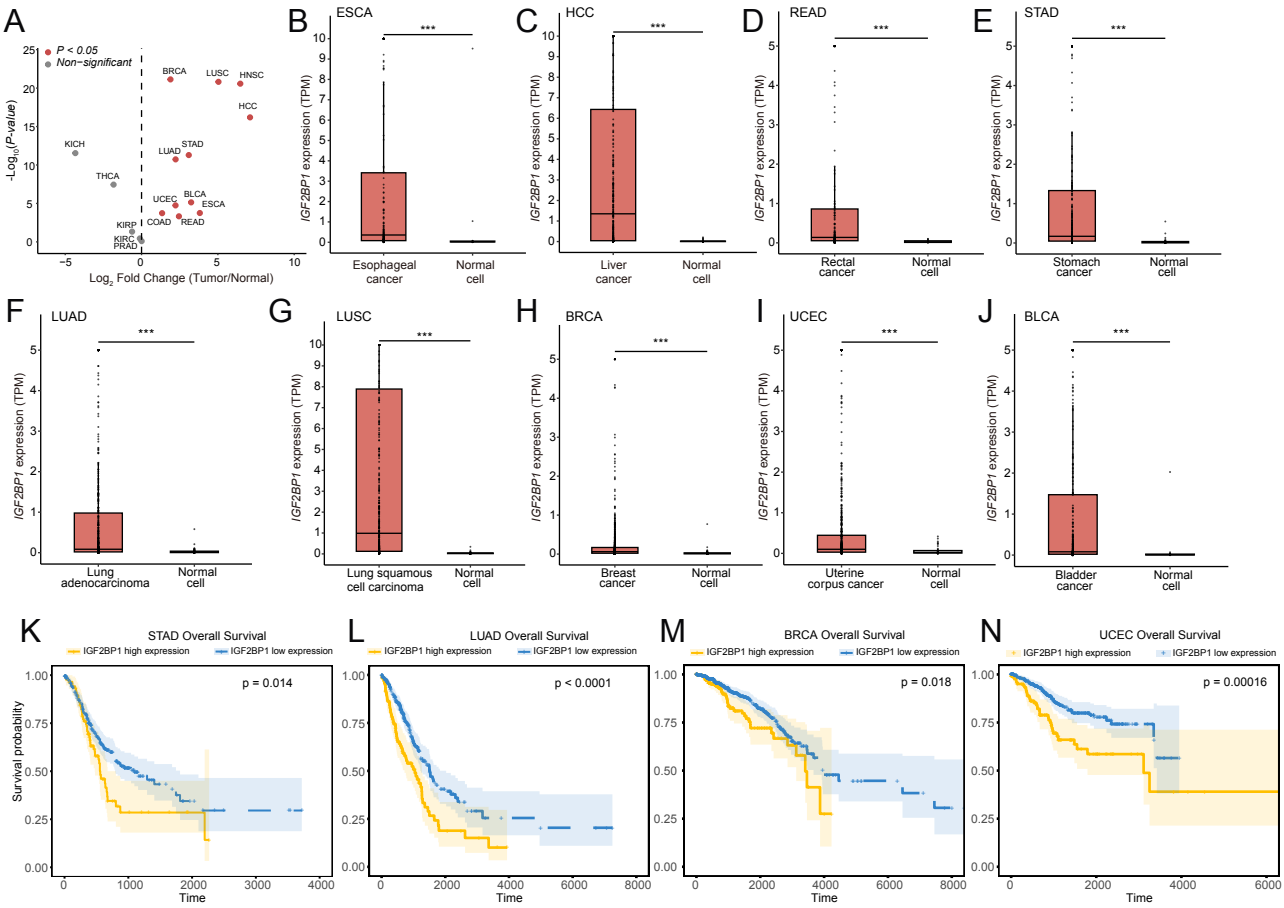
A
P < 0.05
Non−significant
BRCA
LUSC
HNSC
HCC
KICH
LUAD
STAD
THCA
UCEC
BLCA
ESCA
KIRP
COAD
READ
KIRC
PRAD
-Log10(P-value)
Log2 Fold Change (Tumor/Normal)
B ESCA
C HCC
D READ
E STAD
IGF2BP1 expression (TPM)
***
Esophageal cancer
Liver cancer
Rectal cancer
Stomach cancer
Normal cell
F LUAD
G LUSC
H BRCA
I UCEC
J BLCA
Lung adenocarcinoma
Lung squamous cell carcinoma
Breast cancer
Uterine corpus cancer
Bladder cancer
K STAD Overall Survival
L LUAD Overall Survival
M BRCA Overall Survival
N UCEC Overall Survival
IGF2BP1 high expression
IGF2BP1 low expression
p = 0.014
p < 0.0001
p = 0.018
p = 0.00016
Survival probability
Time

Fig. S3

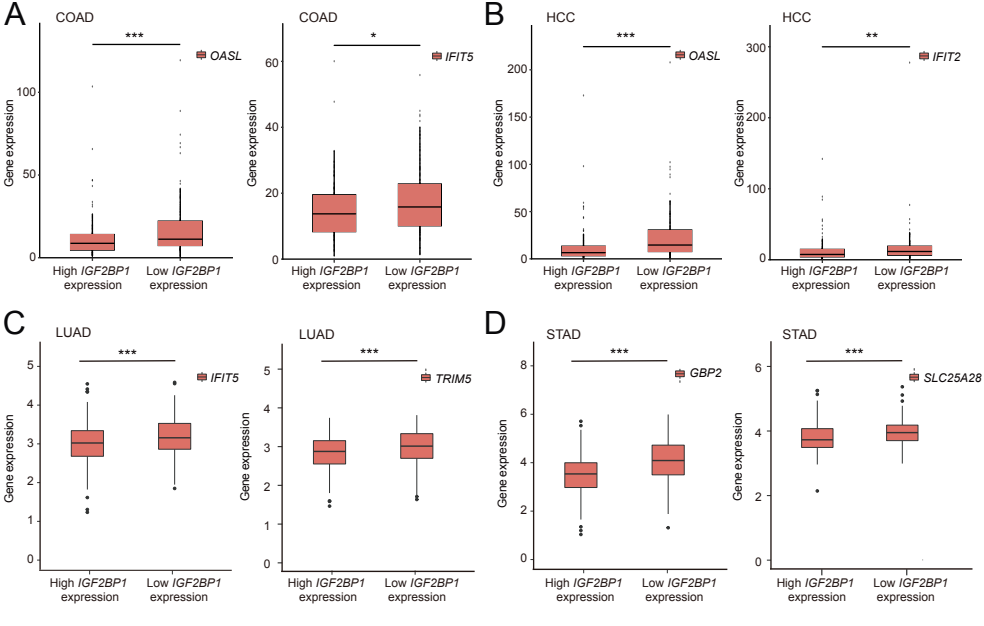
A
COAD
***
OASL
Gene expression
High IGF2BP1 expression
Low IGF2BP1 expression
COAD
*
IFIT5
B
HCC
***
OASL
HCC
**
IFIT2
C
LUAD
***
IFIT5
LUAD
***
TRIM5
D
STAD
***
GBP2
STAD
***
SLC25A28

Fig. S4

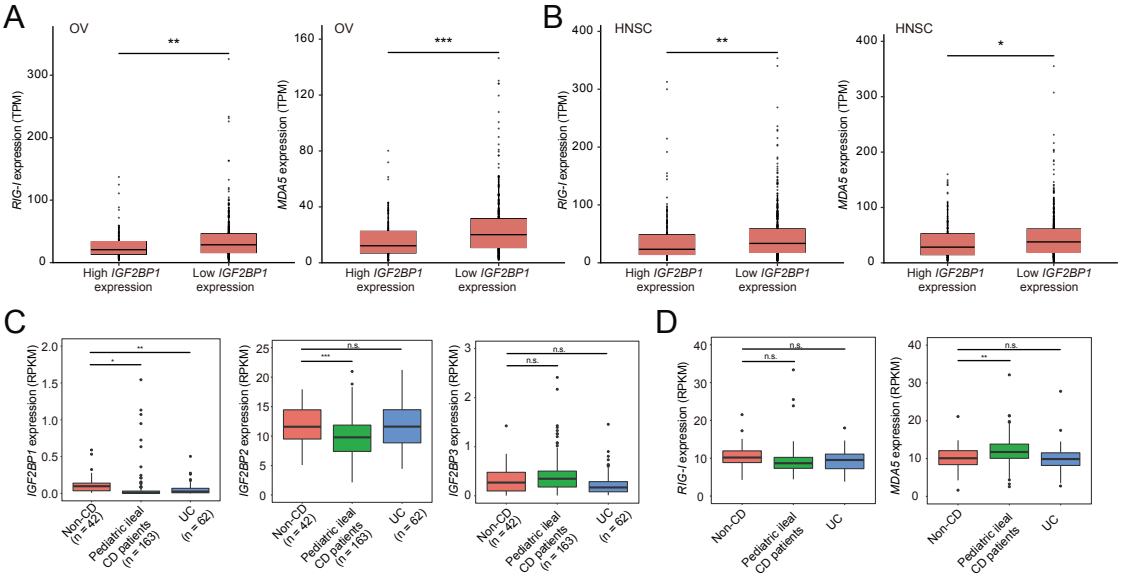
A
OV
**
RIG-I expression (TPM)
0
100
200
300
High IGF2BP1 expression
Low IGF2BP1 expression
OV
***
MDA5 expression (TPM)
0
40
80
120
160
High IGF2BP1 expression
Low IGF2BP1 expression
B
HNSC
**
RIG-I expression (TPM)
0
100
200
300
400
High IGF2BP1 expression
Low IGF2BP1 expression
HNSC
*
MDA5 expression (TPM)
0
100
200
300
400
High IGF2BP1 expression
Low IGF2BP1 expression
C
IGF2BP1 expression (RPKM)
0.0
0.5
1.0
1.5
2.0
**
*
Non-CD (n = 42)
Pediatric ileal CD patients (n = 163)
UC (n = 62)
IGF2BP2 expression (RPKM)
0
5
10
15
20
25
n.s.
***
Non-CD (n = 42)
Pediatric ileal CD patients (n = 163)
UC (n = 62)
IGF2BP3 expression (RPKM)
0
1
2
3
n.s.
n.s.
Non-CD (n = 42)
Pediatric ileal CD patients (n = 163)
UC (n = 62)
D
RIG-I expression (RPKM)
0
10
20
30
40
n.s.
n.s.
Non-CD
Pediatric ileal CD patients
UC
MDA5 expression (RPKM)
0
10
20
30
40
n.s.
**
Non-CD
Pediatric ileal CD patients
UC